

The complex spectral structure of transient LFPs reveals subtle aspects of network coordination across scales and structures.

Michel Besserve^{1,2}, Shervin Safavi¹, Bernhard Schölkopf² and Nikos K. Logothetis^{1,3}

¹Department of Physiology of Cognitive Processes, Max Planck Institute for Biological Cybernetics, Spemannstrasse 38, 72076 Tübingen, Germany.

²Department of Empirical Inference, Max Planck Institute for Intelligent Systems, Spemannstrasse 38, 72076 Tübingen, Germany.

³Centre for Imaging Sciences, Biomedical Imaging Institute, The University of Manchester, Manchester M13 9PT, United Kingdom.

Corresponding Author: Michel Besserve
Spemanstrasse 38,
72076 Tuebingen
Germany
Email: michel.besserve@tuebingen.mpg.de

Keywords: Local field potentials, oscillations, neural events, Neural Event Triggered-fMRI, Hippocampus, Thalamus.

Abstract

Brain Local Field Potentials (LFP) exhibit various dynamical patterns reflecting underlying cooperative network mechanisms at multiple scales that are still largely unexplored in subcortical structures. Such patterns have long been characterized by their activity in various frequency bands. However such decomposition fails to capture fundamental features electrical signals. Using an band free decomposition approach applied to single channel recordings from anesthetized monkey in Hippocampus, we identifies dynamical patterns, such as Sharp Wave-Ripple complexes, and characterizes their brain-wide properties using concurrent fMRI recordings. We also link LFP events to the underlying local activity changes in the recorded structure and show this relationship is highly structure specific. Overall, this approach helps elucidate the relationship between LFP transient activity, the local circuit dynamics and brain-wide interactions.

Introduction

The ability of mammals to react quickly to environmental changes requires their brain circuits, highly interconnected at multiple scales (Abeles, 1982, Honey et al., 2007), to coordinate their activity efficiently. Local Field Potential (LFP) activity, generated by transmembrane currents originating from the cells near to the intracortical electrode tip (Mitzdorf, 1985, Logothetis and Wandell, 2004), is an important marker of neural cooperation as it reflects several local perisynaptic integrative processes (Logothetis, 2008). In particular, transient phenomena, such as rhythmic bursts (Roopun et al., 2008, Wang, 2010, Buzsáki, 2006), or more complex patterns, such as Sharp Wave-Ripples (SPW-R) (Buzsaki et al., 1992), reflect various network mechanisms instrumental to brain function (Buzsáki, 2006, Wang, 2010). Fully characterizing these neural events across time and brain structures would allow decomposing brain activity into sequences of *atoms* of neural computation and greatly help understand the dynamics of neural information processing at a system level (Marcus et al., 2014). To achieve this characterization, classical LFP frequency bands have been established in the clinical electroencephalography and electrophysiology literature, dominated by the study of neocortex and a few other structures. These bands are scrutinized in numerous studies investigating functions as diverse as sleep, perception or motor control.

However, the LFP dynamic patterns and associated mechanisms are highly dependent on the detailed local properties of the network, including the recurrent local organization of canonical microcircuits, synaptic inputs from other brain structures, as well as diffuse neuromodulatory inputs from brainstem and basal forebrain. Not only the above circuit structures affect LFPs by shaping the sequences of excitations and inhibitions of various neuronal types, but also the detailed geometrical arrangement of cells will determine which part of the network activity is be captured by the extracellular electrical field. While these circuit properties show a relative stability across the mammalian neocortex, subcortical regions exhibit a large diversity. As a consequence, studying a subcortical region by scrutinizing its LFP activity in predefined frequency bands might result in a suboptimal, if not misleading, description of relevant activity in this particular structure. In addition, several aspects reflecting the often non-linear properties of the mechanisms generating LFP neural events are not well captured by a decomposition of the LFP signal in fixed frequency bands. In particular, informative aspects of transient neural activity also lies in the more complex features of neural activity, such as harmonics and cross-frequency coupling, showing that LFP activity can involve several frequencies at the same time (Thiagarajan et al., 2010, Abeysuriya et al., 2014a, Canolty et al., 2006, Contreras et al., 1996). These observations call for a general *data-driven* methodology to identify relevant events in LFP data without relying on an *a priori* choice of frequency bands to scrutinize. To overcome the issues of fixed-band LFP analysis, stimulus-informed methods have been introduced for partitioning of the frequency domain (Belitski et al., 2008, Montemurro et al., 2008, Magri et al., 2012), but cannot be used when overt stimuli or behavioral information are unavailable, as it is the case in most sleep and anesthesia studies. One the other hand, independent component analysis techniques or realistic biophysical generative models of LFPs (Makarov et al., 2010,

Einevoll et al., 2007, Schomburg et al., 2014) can extract relevant LFP components with less prior information, but are not appropriate when only one or few recording channels are available.

In the present study, we propose to take advantage of the rich dynamical information available in single channel LFP data to detect all types of dynamical patterns using a two-step methodology. First, LFPs are modeled as a sum of dynamical components, identified by their Power Spectral Density (PSD) profile. Second, we detect frequently occurring temporal patterns in these components using a dictionary learning approach. We apply this methodology to signals recorded with extracellular electrodes in the CA1 area of the hippocampus (denoted Hp along this manuscript) of anesthetized monkeys. This subcortical structure have as privileged relationship to neocortex by reactivating cortical assemblies encoding past sensory experiences (Ji and Wilson, 2007). We use concurrent whole brain functional Magnetic Resonance Imaging (fMRI) recordings to characterize the LFP events according to their associated Blood Oxygen Level Dependent (BOLD) responses in multiple structures, such that both their local and brain-wide properties can be assessed simultaneously. A clustering of the events detected by our approach identifies 6 different neural events in this structure. In addition, the temporal couplings of hippocampal events suggest that the events' occurrences are temporally organized at a supra-second time scale, possibly reflecting a global brain state dynamics. These results illustrate how the specificity of transient LFP neural activity in various brain structures can be quantified using an appropriate identification of relevant neural events. The repertoire of LFP events built in this way will help elucidate how a given brain structure participates in the overall brain activity at multiple temporal and spatial scales.

Results

Dynamical properties of LFP signals

Extracellular potentials from the pyramidal layer of the CA1 region of hippocampus (Hp), or from LGN were recorded simultaneously with whole-brain fMRI in anesthetized monkeys. The detailed experimental setup has been previously described in (Logothetis et al., 2012) (see Materials and Methods). As illustrated in Figure 1a, the LFP time-course undergoes fast changes in its spectral content over time as witnessed by the occurrence of oscillatory bursts at different time scales. Such changes can be captured with low run time complexity by computing the Short Term Fourier Transform (STFT) spectrogram, also represented on Figure 1a. Bursts of high and low frequency oscillations appear at different locations of the spectrogram (see Figure 1a, orange and green rectangles respectively). The occurrence of such transient brain rhythms has been reported in a large number of brain structures and species (Buzsáki and Draguhn, 2004) and associated to various underlying mechanisms (Brunel and Wang, 2003, Contreras et al., 1996). Interestingly, Figure 1a also shows increases in the magnitude of the spectrogram involving broader frequency ranges (purple rectangle). The variety of transient spectral profiles observed in this example LFP time series likely reflects different underlying cooperative mechanisms as

supported by modeling and experimental studies. For example, recurrent interactions within and between populations of excitatory and inhibitory neurons in local cortical microcircuits generates high frequency oscillations in the LFP (Brunel and Wang, 2003) (Figure 1b, orange arrows). Alternatively, post-synaptic currents generated by a volley of synchronous action potentials in a remote afferent brain region typically result in slower LFP waveforms (Buzsaki, 1986) (Figure 1b, green arrows). More generally, combinations of such local and long-range interactions can generate more complex LFP patterns involving a broad range of frequencies. As a consequence, our approach to discover cooperative mechanisms in a recorded brain structure relies on detecting transient LFP activities characterized by specific spectral profiles and further study their properties.

Time varying spectral decomposition of LFPs

To identify these profiles efficiently, the STFT spectrogram matrix shown in Figure 1a is modeled as a linear superposition of a few spectral profiles associated to the different underlying events. Across time, each spectral profile is assumed to keep the same shape, but its contribution to the spectrogram can vary in magnitude. Stated in this form, retrieving these spectral profiles from data can be cast as a Non-negative Matrix Factorization problem (NMF) (Seung and Lee, 2001). Let \mathbf{S} be the (frequency x time) spectrogram matrix, NMF seeks optimal matrices \mathbf{W} and \mathbf{H} having only positive coefficients and such that:

$$\mathbf{S} \approx \mathbf{WH} \quad (1)$$

The number of columns of \mathbf{W} is the same as the number of lines of \mathbf{H} and sets the assumed number of spectral profiles K appearing across time in the data. As illustrated in Figure 1c, while the columns of \mathbf{W} correspond to the spectral profile of each of these components, the lines of \mathbf{H} are weights quantifying the time-varying contribution of the spectral profiles to each time window. The NMF problem is solved by minimizing a dissimilarity measure called *divergence*, quantifying how close the factorization on the right-hand side of Equation 1 is to the original spectrogram matrix (Seung and Lee, 2001, Févotte et al., 2009, Sra and Dhillon, 2005). While the Euclidean norm is the simplest and most widely used divergence, we argue that NMF based on the Itakura-Saito divergence (IS-NMF), previously used in music analysis (Févotte et al., 2009) is particularly suited to LFP analysis due to its scale invariance properties (see Supplementary Methods). This allows the method to automatically adapt to the typical “ $1/f$ ” distribution of the PSDs observed in neural time series (Novikov et al., 1997, He et al., 2010) and illustrated by the decrease of spectrogram values with increasing frequency in Figure 1a. As a consequence, IS-NMF can better detect low power high frequency spectral profiles frequently observed in empirical LFP data, as illustrated in simulations in Supplementary Results and Supplementary Fig. 1. In addition, the IS-NMF approach allows for a probabilistic modelling of the original signal, which associates NMF results to a decomposition of the original time series into dynamical components (Smaragdis et al., 2014) that we will exploit in later sections.

The outcome of IS-NMF for the recordings shown in Figure 1a using 3 components is also represented in Figure 1c. The estimated spectral profiles (normalized by their maximum value) show that IS-NMF captures various aspects of neural activity altogether covering a wide range of frequencies (from 2-150 Hz). The time-varying contribution of the spectral profiles exhibit isolated peaks corresponding to the occurrence of transient events in the LFP.

Classification of spectral components in hippocampus and LGN

To compare the components detected by IS-NMF in Hp and LGN, we ran the algorithm on several sessions (21 for Hp recordings, 11 for LGN recordings), each of them consisting in 10-20 experiments of 10 min recordings of spontaneous activity. The number of spectral profiles in the NMF decomposition is a parameter subject to trade-off: a large number of components leading to a finer description of neural activity, but at the expense of a larger number of samples necessary to robustly estimate the solution. We assessed the robustness of the decomposition with cross-validation and chose the largest number of components which across sessions led to an average cosine similarity between cross-validated spectral profiles above 80% (see Materials and Methods). The optimal number of 4 components was found for Hp, while 3 components were optimal for LGN (see Supplementary Fig. 2a-b). To analyze the properties of the resulting profiles across sessions, they were pooled together and then clustered (using the above mentioned optimal number of profiles as the number of clusters) based on their pairwise cosine similarity using the normalized cut graph clustering algorithm (Shi and Malik, 2000). The NMF outcome of a few sessions showing components reflecting artifact contamination (recognizable in the spectral profiles by the presence of sharp peaks distributed over a wide range of frequencies) were excluded from this clustering analysis (4 out of 21 for Hp, 1 out of 11 for LGN). The characteristics of the resulting clusters of spectral profiles are summarized on Figure 1d-e. The normalized spectra of Hp clusters are shown in Figure 1d, exhibiting a low frequency component (in blue), as well as several spectra having most of their energy in a specific frequency band: 15-40 Hz, 40-90 Hz, and finally 90-140 Hz. In comparison, the three LGN clusters, computed with the same clustering technique, are shown on Figure 1e and consist in one low frequency component (<15 Hz), one component with most of its energy in a narrow band (15-25 Hz), as well as a broad high frequency component (25-130 Hz). In comparison to Hp components, LGN spectral profiles thus extend to a lower frequency range, suggesting differences in the underlying network dynamics of these structures. The observed transient spectral profiles describing neural activity can differ in many respects, which are not only limited to their peak frequency. Previous modeling studies have shown that the non-linear properties of the underlying neural network can affect the shape of the PSD of the observed neural time series, for example by generating harmonics at multiples of the peak frequency (Abeywuriya et al., 2014a, Abeywuriya et al., 2014b, Breakspear et al., 2006, Robinson et al., 2002). While a more detailed study of these spectral properties is left to further studies, we characterized our spectral profiles using two simple parameters: their peak frequency and their spectral centroid (see Supplementary Methods). Spectral centroid measures the center of mass of the spectral profile distribution across frequencies. As a consequence, the closer it gets to the

peak frequency; the closer is the spectral profile to a single narrow-band peak deprived from harmonics, and the closer is the associated time course to a sinusoid (see illustration Figure 1f, more details are provided in Supplementary Methods and Supplementary Fig. 3). Hence, we call the ratio of the spectral centroid to the peak frequency the *spectral purity ratio* and use it to quantify putative non-linear network interactions associated to each profile (see results Fig. 1g-h). Interestingly, the spectral purity ratio was higher for LGN spectral profiles than for Hp profiles ($p < 10^{-4}$, one-sided Wilcoxon rank sum test, $n=81$), suggesting more prominent non-linear network dynamics in LGN.

Time course of dynamical components

While IS-NMF results provide an overview of the spectral profiles present in LFP data, it is important to understand how such profiles contribute to the time course of neural activity and whether they can be interpreted in terms of known phenomena. One important feature of the IS-NMF decomposition is to associate a time course to each spectral component according to the Gaussian Composite Model (Févotte et al., 2009, Smaragdis et al., 2014), leading to a linear decomposition of the LFP signal into a sum of dynamical components in the time domain (see Supplementary Methods). After applying an invertible decomposition of the signal into blocks using overlapping tapering windows (Allen, 1977), the time course of each component can be estimated efficiently for each block based on NMF results by using a time varying filter bank. In practice, as illustrated in Figure 2a-b, normalized NMF profiles for a given time window define the filter bank applied to the LFP in the Fourier domain to generate the time courses of each dynamical component. This approach is performed on successive overlapping time windows and the full time course of each component is reconstructed by simply summing the contribution of all windows as illustrated in Figure 2c.

In Figure 3a-b, we represent examples of the estimated time course of dynamical components for Hp and LGN recordings respectively. It can be seen that while events are difficult to identify in the LFP traces, each component exhibits occurrences of stereotypical patterns, some of which appearing sinusoidal (Figure 3a green component), while others exhibit more complex shapes (Figure 3a cyan component). This decomposition thus helps us detecting potentially interesting neural events and their characteristics. To detect such events automatically, we apply to each component a shift-invariant dictionary learning technique inspired by work in music analysis (Mailhé et al., 2008). This approach approximates each time series by a superposition of shifted and rescaled typical patterns appearing in the time course. The recursive estimation of these patterns is schematized in Figure 3c and explained in Materials and Methods (see also the simulation study in Supplementary Results). The method parameters were chosen in cross-validation (see Supplementary Methods). Figure 3a-b shows the resulting detected events surrounded by colored rectangles and the estimated dictionary patterns of each dynamical component are shown on Figure 3d-e for Hp and LGN examples shown in Figure 3a-b respectively. Interestingly, it is possible to identify among detected patterns important events reported in the literature as hippocampal SPW-R (Figure 3a top component). Being able to detect

these events with our approach is particularly interesting because it is a compound of a low frequency waveform, the sharp wave and a high frequency oscillation, the ripple. It thus shows the capability of the reconstruction technique to detect patterns with complex (non-sinusoidal) time course corresponding to non-linear dynamical interactions.

Local and brain-wide neural event properties

The LFP neural events, although detected at a single recording site, likely reflect mechanisms engaging a broader set of structures. We take advantage of the simultaneously recorded fMRI signal to compute the Neural Event Triggered(NET)-fMRI activity in cortical and sub-cortical Regions of Interest (RoI) to assess how the occurrence of a neural event relates to metabolic changes in various brain structures (see illustration Figure 4a and Materials and Methods). We first computed the magnitude of the NET-fMRI responses following event onset in two broad brain regions that were relevant in previous studies : neocortex and thalamus (Logothetis et al., 2012) (see Materials and Methods). The raster plot of thalamic response against cortical response are represented Figure 4b respectively. These plots show a clear and significant negative correlation between thalamic and cortical response (Spearman: $\rho = - .855$, $p < 10^{-7}$). Detected Hp events thus tend to have opposite metabolic correlates in neocortex and thalamus, extending previous observations regarding hippocampal SPW-R (Logothetis et al., 2012). We checked that this effect could not be explained by an overall negative correlation between the two structures. As shown in Figure 4f, the distribution of correlation between fMRI recordings from thalamus and cortex has a positive median (Wilcoxon signed rank test, $p < .001$), and thus cannot account for the opposite signs of thalamic and cortical responses during hippocampal events. These results support that events detected in Hp reflect competitive interactions between neocortex and thalamus, and we quantify this property for each individual event by defining a *Thalamocortical Competition Index* (TCI) as the algebraic coordinate of each point projected in Figure 4b along the regression line relating thalamic to cortical response. Large positive TCI values (towards bottom right) represent events with large positive cortical response and large negative thalamic response, while negative values reflect the opposite effects. According to the sign of TCI, we split all our observed events in two categories: the cortex-activating (CA) events, with positive TCI, and the thalamus-activating (TA) events, with negative TCI. We then analyzed the properties of these categories separately by applying a clustering procedure on each subset based on the peak frequency of the Fourier transform of their dictionary pattern (see Materials and Methods). The optimal number of clusters was chosen according to the silhouette index (Desgranges, 2013) (see Materials and Methods). To overview together the brain-wide and local properties of the clustered events, we show in Figure 4c their corresponding dictionary patterns, mapped according to the magnitude of their TCI as well as the peak frequency of their LFP dictionary pattern. CA patterns were clustered in 3 subtypes, associated to LFP activity in lower frequencies (median peak frequency of 4.5 Hz), the classical EEG alpha band (10.0 Hz median frequency peak) and the classical EEG beta band (median peak frequency 21.9 Hz). The CA clusters are also in the number of 3. Two of these clusters (Clusters 5 and 6) correspond to low gamma and ripple events according to their median peak frequencies at 37.5 Hz and 94.3 Hz

respectively, and are associated to strong cortical activation and thalamic deactivation, as previously reported (Logothetis et al., 2012). The additional CA event subtype (Cluster 4), has a frequency range similar to Cluster 1 (4.5 Hz median peak frequency). However, one can notice in the dictionary patterns belonging to this cluster an additional high frequency oscillation, as illustrated by the magnified example pattern of Figure 4c.

To better understand this exception, we assessed in more detail the neurophysiological differences between low frequency cortex-activating Hp events from their thalamus-activating counterpart. We thus computed the neural event triggered average of the LFP spectrogram (see Materials and Methods) for all Hp events. The average of these spectrograms across clusters, showing the frequency content of LFPs specific to each cluster in a peri-event time window, are shown on Figure 5a. While all spectrograms exhibit a peak in power at event onset around previously measured median peak frequency, we observe that Hp Cluster 4 has an additional high frequency peak (157 Hz peak frequency), corresponding to the previously observed oscillation apparent in the dictionary patterns (see example Figure 5a). This event cluster thus clearly corresponds to hippocampal SPW-R events (Buzsaki et al., 1992, Ylinen et al., 1995), paradigmatic of neural events involving multiple frequencies.

While events have been found to fall in two categories, CA or TA, their brain-wide properties might differ in other respects, reflecting differences in brain-wide network interactions. To check in more detail the differences between large scale metabolic changes associated to each Hp event cluster, we plot the average time course of NET-fMRI responses in two representative brain structures (Figure 5b). While the three TA event subtypes, have in common a deactivation in cortical structures, some NET-fMRI responses deviate above 0 before the stimulus onset (see green arrow in Figure 5b). We quantified the significance of this pre-activation phenomenon in cortex by averaging the responses across all cortical RoIs over a period of 6s preceding stimulus onset. The distribution of average NET-fMRI pre-activation magnitudes for TA clusters is represented on Figure 6a. Interestingly, only the events with lower frequency oscillation patterns (Cluster 1) show significant cortical pre-activation according to a Wilcoxon signed rank test ($p < .01$, Bonferroni corrected), which suggests this low frequency event might not emerge spontaneously from hippocampus, but would rather be caused by earlier changes in brain activity.

Event temporal dynamics

While the fMRI correlates of neural event clusters were analyzed independently in the above section, their occurrence might be linked dynamically; making two types of events more probable to occur in close temporal proximity. Such dynamical coupling may in turn relate to the NET-fMRI results observed above in the case of Hp events. In particular, the similarity between the NET-fMRI responses associated to each CA events might reflect the occurrence of these different events in close temporal proximity. In addition, the cortical pre-activation phenomenon observed for Hp cluster 1 could be due to the occurrence of a CA event several seconds before event onset. To test these conjectures, we computed the time resolved conditional intensities (or

second order intensity) of one type of event (the number of events occurring per time unit) given a “conditioning” event of a given type occurs at time zero (Brillinger, 1976). While the overall conditional intensity plots for all possible event pairs are provided in Supplementary Fig. 8, Figure 5 c provides key example of dynamic coupling between ripples and other events. First, as previously observed (Logothetis et al., 2012), the detected ripples have a significant probability to occur in sequences. This is validated by the increased ripple intensity in the neighborhood of a ripple event onset. In addition, ripples have also more chances to occur in close neighborhood to Sharp-waves. This confirms the classical result that Sharp-waves and ripples frequently occur together, although not systematically (Ramirez-Villegas et al., 2015). Overall, there is a considerable coupling between the occurrence of all CA events in Hp, possibly explaining the similarity between the NET-fMRI signatures of sharp-waves, ripples and gamma oscillations. In addition, among CA events, ripples have specifically more probability to occur before lower frequency oscillation (cluster 1). This again provides a putative explanation for the cortical pre-activation associated to low frequency oscillations. Overall, the NET-fMRI responses may not only reflect the activity related to a given isolated event, but also the metabolic changes due more broadly to the sequences of events occurring in multiple structures, that are dynamically linked to the detected event.

Local neural activity during neural events

We observed a similarity of the relationship between brain wide fMRI activity and LFP patterns in two subcortical structures: high frequencies are related to an increase in the neocortical BOLD signal. Previous results from LFP recordings in primary visual cortex (Logothetis et al., 2001, Murayama et al., 2010), showed that high frequency LFP activity was in good correspondence with the BOLD signal in the tissue surrounding the recording site, and a better predictor of the fMRI signal than spiking activity estimated using the MUA signal. To investigate whether the relationship of LFP patterns to the underlying local neural activity is similar in subcortical structures recorded in the present study, we use two quantifications of neural activity: on the one hand the amount of multi-unit spiking in the underlying populations measured electrophysiologically, and on the other hand the metabolic activity measured by the BOLD signal. To quantify the massed firing rate in the neighborhood of the electrode, we extracted the Multiple Unit Activity (MUA) signal by filtering the extracellular signal in the (800-3000 Hz) frequency range and rectifying it. The distribution of average MUA activity changes in a 400ms peri-event time window (excluding a 10ms peri-event window to avoid artifacts due to event detection), Z-scored with respect to randomized events, are shown for each event clusters in both structures on Figure 6c and 6d respectively. Local metabolic activity changes are quantified as in the previous section, using the magnitude of the NET-fMRI responses (see Material and Methods) in the manually labeled ROI associated to each structure where the electrode is located, namely LGN and Hippocampus. Distributions of local metabolic changes for each event clusters are shown for each structure on Figure 6e and 6f. Interestingly comparison of MUA and local metabolic activity show similar trends, significantly positive metabolic changes corresponding to significant MUA increases. On the other hand, other events do not appear to have significantly

negative metabolic changes (although median values are negative), and are related to no significant changes in MUA activity. Most importantly, there is a clear relationship between local activity changes and the TA/CA property of events in both structures, but with a major difference. While CA events lead to the largest increase in local activity in Hp, TA events are the ones reflect increase in local activity in LGN. This implies that LFP events in similar frequency bands have a largely structure dependent relationship to the underlying level of local activity. In particular, these results suggest that low frequency (below 25Hz) events relate to local metabolic increases in LGN, but not in Hp. Overall, the results emphasize that the local network properties associated to neural events are largely structure dependent.

Neural events in the model of thalamocortical system

In order to investigate, to what degree the detected neural events are informative about the cellular processes (e.g. membrane potentials and ionic currents), we exploit a simulation of thalamocortical system developed by (Costa et al., 2016). The putative relationship between neural events and cellular dynamics is import from two aspects. First, presence of a relationship between neural events and cellular dynamics signify the fact that neural events are not just statistically important pattern in the LFPs, but also they can be mechanically meaningful. Second, presence of a relationship adds another piece of evidence that neural events, not only provide us a time window that meso-scale dynamics is closely related to macro-scale dynamics (Logothetis et al., 2012), but also the micro-scale dynamics of the brain.

We identify neural events in the membrane potential of excitatory population only in the thalamus module (Figure 6a), as a crude proxy of LFP signal (see the method section for the justification). Applying our method on approximated LFP (will be called briefly LFP rather approximated LFP in the remaining of this section for the simplicity) led to 3 types of neural events (Figure 6b) depict LFP surrounding the exemplary of each neural event). Interestingly, two of the identified events are the well-known type I and type II thalamic spindles.

Further analysis of the cellular dynamics in the vicinity of the neural events with high amplitude (determined based on dictionary learning), suggests that each neural event has a distinct profile cellular dynamic. We build a large feature vector from the time course of all membrane potentials and the calcium current surrounding the neural events and reduce its dimensional with t-distributed stochastic neighbor embedding (tSNE) (van der Maaten et al. 2008). Interestingly, a 2-dimensional representation the cellular dynamics underlying neural event demonstrate clear clusters (Figure 6c).

Discussion

Neural information processing relies on cooperative phenomena which manifest themselves in the complexity of recorded brain signals. We introduced a principled approach to exploit the dynamical properties of single channel LFPs to detect these phenomena with minimal prior

assumptions. Two key features of this approach are that it does not rely at all on band-pass filtering of the signals, and that it associates to each detected event a time resolved pattern of activity. Compared to analysis in predefined frequency bands, these features are beneficial for electrophysiology data analysis and modeling purposes, as they avoid mixing the effects of different types of events, such as CA and TA events, which would result from choosing a frequency band that is not adapted to the data at hand. In addition, this approach facilitates the interpretability of the results, as it can automatically capture non-linear properties of events, such as the involvement of several frequencies in Sharp-Wave Ripples, and computes typical temporal patterns of the events that are easily identifiable in the LFP time course. Such results can be further exploited in modelling studies in order to guide the design of the network mechanisms that generate such LFP properties (see also Supplementary Discussion for additional discussion regarding the chosen approach).

We applied this methodology to ongoing macaque LFP recordings in two structures: hippocampus and LGN and were able to detect and characterize previously reported phenomena without any prior knowledge. Since whole-brain fMRI activity was recorded concurrently with electrophysiology, we studied the large scale brain activity during the detected events. We used the NET-fMRI methodology (Logothetis et al., 2012) to quantify the level of activation or deactivation related to each event in a large variety of cortical and subcortical RoIs. In line with earlier results focused on SPW-R events (Logothetis et al., 2012), the detected events in both structures reflect a competition between cortical and subcortical regions. While the mechanisms and functional role of this thalamo-cortical competition are yet unknown, we speculate that the large variety of neuromodulatory inputs to thalamus may be involved (Varela, 2014), and that such mechanism can avoid different information processing pathways to interfere. In particular, the replay of memory traces in cortex triggered by hippocampal SPW-R (Ji and Wilson, 2007) should not be altered by sensory information reaching cortex through thalamic relays to ensure correct encoding of those memories. Importantly, the observed thalamo-cortical competition is specifically related to the events observed in the recorded subcortical structures, as the fMRI signals in cortex and thalamus are overall positively correlated when considering the whole time course. This suggests that for each type of event occurring in a brain structure, it is possible to associate information routing pathways that links the activity of this structure to the overall brain activity. Interestingly, the relationship of LFP rhythms (excluding SPW-R complexes) to brain-wide metabolic changes share common features in Hp and LGN structures, higher frequencies being related to cortical activation and lower ones to thalamic activation. In addition, lower frequency events in both recorded structures were associated to metabolic changes in cortex prior to the onset of the event, suggesting that these events may be triggered by other events happening earlier in the neocortex.

In contrast to their effect on cortex, the relationship between the frequency of LFP events and the underlying activity in the structure in which LFPs are recorded is more structure specific. While previous work in the visual cortex has shown that high frequency oscillation was reliably

associated to spiking as well as BOLD signal increases (Murayama et al., 2010, Logothetis et al., 2001), we observe a similar relationship in Hippocampus but not in LGN. In contrast, low frequency events (below 25Hz) are the one associated with an increased activity. This finding is supported by experimental studies reporting a decrease in LGN beta band power (20-40Hz) during visual stimulation while lower frequencies (7-15Hz) were increasing (Bastos et al., 2014), suggesting information processing in LGN is associated with increased lower frequency activity. In principle, possible explanations for such discrepancies of the relationship between LFP, fMRI and population spiking activity pertaining to the microcircuit anatomical and functional organization have been reviewed in Logothetis (2008).

The nature of the higher frequency events (above 25Hz) that we detect in LGN, as well as thalamus activating lower frequency events in CA1, remains elusive and requires further experimental and modeling studies. All these events have in common to be associated with weak local BOLD and spiking activity, suggesting that they correspond to mainly subthreshold mechanisms. This subthreshold activity might be strongly influenced by synaptic and neuromodulatory inputs for other brain structures. For example low frequency activity in hippocampus might reflect the synaptic filtering of neocortical delta and spindle oscillations. In support of this view, delta and spindles are associated to an electroencephalographic pattern, the K-complex, associated to neocortical down-states (Cash et al., 2009) and thereby justifying the neocortical down-regulation associated to these events. Connecting the occurrence of these events to brain state fluctuations may also explain the cortical pre-activation observed in our NET-fMRI results and the increase probability of ripples to occur several seconds prior to low frequency events. Indeed, ripples reportedly occur more frequently during down- to up-state transitions during slow-wave sleep (Battaglia et al., 2004) while lower frequencies would then be associated to the following up- to down-state transitions. Overall, these results illustrate how our approach to extract neural events allows a detailed study of large scale network interactions and their largely unexplored underlying mechanisms concurrently happening in multiple brain structures.

Materials and methods

Surgical procedures, electrophysiology and fMRI recordings

Experimental and surgical procedures have been detailed in a previous study (Logothetis et al., 2012). In summary, a total of 24 recording sessions were carried out in 4 anesthetized male rhesus monkeys (*Macaca mulatta*). Head holders and recording chambers were located stereotactically based on high-resolution anatomical MRI scans. Hippocampal recordings were conducted in the anterior part of the hippocampus in the right hemisphere of each animal. Additionally, thalamic recording were recorded in the Lateral Geniculate Nucleus (LGN) in some animals in the same hemisphere. All recording hardware, including the electrodes and amplifiers for simultaneous fMRI and multi-site electrophysiology recordings, was developed at the Max Planck Institute for Biological Cybernetics. Multi-contact recordings were performed

around the pyramidal layer of the hippocampal CA1 subfield (8 to 14 mm anterior of the interaural line). Fine adjustment of the recording electrode was achieved by intermediate MRI anatomical scans. Functional imaging was carried out in a vertical 4.7 Tesla scanner, in which each animal was positioned in a custom-made chair. Typically, 22 axial slices were acquired, covering the entire brain. BOLD activity was acquired at a resolution of 2 seconds. During all experiments, anesthesia was maintained with remifentanil (0.5-2 µg/kg/min) in combination with a fast-acting paralytic mivacurium chloride (5-7 mg/kg/h), only mildly affecting the magnitude and time course of neural and vascular responses (Logothetis et al., 2012, Goense and Logothetis, 2008). All experimental and surgical procedures were approved by the local authorities (Regierungspräsidium, Tübingen Referat 35, Veterärwesen) and were in full compliance with the guidelines of the European Community (EUVD 86/609/EEC) for the care and use of laboratory animals.

Processing and Analysis of Neural Data

Analyses of electrophysiology and fMRI data were performed using MATLAB (The MathWorks). LFP data was cleaned from electromagnetic gradient artifacts, down-sampled and low pass filtered at 660 Hz (Logothetis et al., 2012). In addition to anatomical criteria, we selected in each recording session one hippocampal recording tip belonging to stratum pyramidale (PL) based on the relative power in the ripple band (100-200 Hz). In each session containing thalamic recordings, we chose the recording tip in LGN having the maximum multi-unit response to a polar checkerboard stimulus.

Overlap-add decomposition and short term Fourier analysis

Spectrogram analysis was performed on the LFP time series by tapering the signal using sliding 600ms Hanning windows with 50% overlap. Tapering windows were normalized such that at any time point, the sum of overlapping tapering windows is one, which ensures an exact reconstruction of the time course of the original signal based on short-term Fourier transform values using the overlap-add technique. The tapered signal was then Fourier transformed using the FFT algorithm and squared to get the spectrogram values for this window.

Non-negative matrix factorization

The IS-NMF algorithm was applied to the spectrogram matrix obtained according to the previous paragraph. The factorization was initialized by drawing spectral profiles at random using uniformly distributed coefficient on the unit interval, and the corresponding time contributions were initialized using least square regression (see Supplementary information). The NMF decomposition was then optimized using the multiplicative update algorithm (Sra and Dhillon, 2005) and the stability of the solution was enforced using an iterative bootstrap approach to find a good initialization of the components (see Supplementary Methods). To determine an optimal number of components, the robustness of the result was assessed by cross-validation using two subsets of experimental recordings (with 50% overlap): the spectral profiles obtained by the approach using these two subsets were matched and compared using the cosine

similarity. The average cosine similarity between the matched spectral profiles resulting from each subsets was used as an indicator of the robustness of the result.

Dictionary learning

The principle of this approach is illustrated in Figure 3c. After initialization by random patterns, the algorithm alternates between a Matching Pursuit step, which detects iteratively the event locations by finding the time points where the component time course has maximum similarity with one of the dictionary patterns, and an Singular Value Decomposition (SVD) step in which the dictionary patterns are updated by computing the singular vector of largest singular value of the matrix gathering all peri-event time windows of the component's time series at locations where a given pattern was detected. Good convergence of the algorithm was reached after 30 iterations. The shift-invariant dictionary learning procedure has two free parameters: the number of dictionary patterns and the total number of events to detect. These parameters were selected using a cross-validation procedure described in Supplementary Methods. The performance of the approach was also evaluated in Supplementary Results.

Clustering of Neural Events

Neural events were clustered according to the peak frequency of the Fourier transform of their associated dictionary pattern. We excluded from this analysis events with residual MRI artifact contamination, that we detected using their peri-event LFP spectrogram: the Fourier transform of the spectrogram time course averaged over higher frequencies (133-300 Hz) and the corresponding event was excluded whenever the magnitude absolute Fourier transform at its peak frequency was larger than three times the average magnitude of the Fourier transform at the frequencies surrounding the peak frequency. Events with their peak frequency within [49-51 Hz], corresponding to line noise were also excluded from this analysis. We defined a distance between two events as the absolute difference between the two frequencies, normalized by their maximum. We subtract this distance to 1 to define a similarity measure which is used to cluster events using a graph clustering procedure (Shi and Malik, 2000). To avoid outliers to bias the clustering procedure, events having less than 2 neighbors within a distance of less than .2, were also excluded from the procedure. This approach was repeated for a number of clusters ranging from 2 to 12, the quality of the clustering for each number of clusters was assessed using the silhouette index based again on the same distance metric. The silhouette index quantifies how grouped the clusters are within each cluster with respect to the whole dataset (Rousseeuw, 1987). We evaluated the graph of the silhouette index against the number of clusters, and selected the smallest number of clusters achieving a local maximum of this graph.

Neural Event triggered measures

To characterize local and large scale properties of neural events, we computed two quantities: NET-fMRI and spectrogram, based on the peri-event time course of the fMRI and LFP signal respectively. NET-fMRI maps were computed by averaging the peri-event time course ranging from 20 second before event onset until 20 second after event onset. Peri-event signals were preliminarily detrended. Spectrograms were estimated by first computing the continuous wavelet

transform with a complex Morlet wavelet on a 2 second interval centered on each event onset. The spectrogram values were obtained by averaging the squared modulus of the wavelet transform across events. Both quantities were normalized by computing a z-score with respect to randomized events in the following way. Randomized event were generated on each 10 min experiment by taking the original event time stamps, compute the empirical distribution of inter-event intervals, and randomly drawing with replacement from this distribution the same number of intervals as the original. Time stamps of randomized events were generated by picking at random and initial point in the first 20s of the recording and iteratively adding the randomized inter-event intervals.

Descriptive statistics and tests

In figures describing statistics with boxplots, on each box, the top and bottom are the 25th and 75th percentiles of the samples, respectively; the line in the middle of each box indicates the sample median; the dashed lines extending below and above each box are drawn from the ends of the interquartile ranges to the furthest observation (extreme points not considered as outliers); crosses (if any) in the diagrams indicate outliers of the samples. A data point is considered as an outlier whenever it is larger than $Q3+1.5*(Q3-Q1)$ or smaller than $Q1-1.5*(Q3-Q1)$, Q1 and Q3 indicating the 25th and 75th percentiles, respectively. If not specified, statistical tests presented in text and figures are two-sided.

References

- ABELES, M. 1982. *Local cortical circuits: An Electrophysiological study*, Springer.
- ABEYSURIYA, R. G., RENNIE, C. J. & ROBINSON, P. A. 2014a. Prediction and verification of nonlinear sleep spindle harmonic oscillations. *J Theor Biol*, 344, 70-7.
- ABEYSURIYA, R. G., RENNIE, C. J., ROBINSON, P. A. & KIM, J. W. 2014b. Experimental observation of a theoretically predicted nonlinear sleep spindle harmonic in human EEG. *Clin Neurophysiol*, 125, 2016-23.
- ALLEN, J. B. 1977. Short term spectral analysis, synthesis, and modification by discrete Fourier transform. *Acoustics, Speech and Signal Processing, IEEE Transactions on*, 25, 235-238.
- BASTOS, A. M., BRIGGS, F., ALITTO, H. J., MANGUN, G. R. & USREY, W. M. 2014. Simultaneous recordings from the primary visual cortex and lateral geniculate nucleus reveal rhythmic interactions and a cortical source for gamma-band oscillations. *J Neurosci*, 34, 7639-44.
- BATTAGLIA, F. P., SUTHERLAND, G. R. & MCNAUGHTON, B. L. 2004. Hippocampal sharp wave bursts coincide with neocortical up-state transitions. *Learning & Memory*, 11, 697-704.
- BELITSKI, A., GRETTON, A., MAGRI, C., MURAYAMA, Y., MONTEMURRO, M. A., LOGOTHETIS, N. K. & PANZERI, S. 2008. Low-Frequency Local Field Potentials and Spikes in Primary Visual Cortex Convey Independent Visual Information. *J Neurosci*, 28, 5696-5709.
- BREAKSPEAR, M., ROBERTS, J. A., TERRY, J. R., RODRIGUES, S., MAHANT, N. & ROBINSON, P. A. 2006. A unifying explanation of primary generalized seizures through nonlinear brain modeling and bifurcation analysis. *Cereb Cortex*, 16, 1296-313.
- BRILLINGER, D. R. 1976. Estimation of 2nd-Order Intensities of a Bivariate Stationary Point Process. *Journal of the Royal Statistical Society Series B-Methodological*, 38, 60-66.

- BRUNEL, N. & WANG, X.-J. 2003. What Determines the Frequency of Fast Network Oscillations With Irregular Neural Discharges? I. Synaptic Dynamics and Excitation-Inhibition Balance. *Journal of Neurophysiology*, 90, 415-430.
- BUZSAKI, G. 1986. Hippocampal sharp waves: their origin and significance. *Brain Res*, 398, 242-52.
- BUZSÁKI, G. 2006. *Rhythms of the Brain*, Oxford University Press.
- BUZSÁKI, G. & DRAGUHN, A. 2004. Neuronal oscillations in cortical networks. *Science*, 304, 1926-1929.
- BUZSAKI, G., HORVATH, Z., URIOSTE, R., HETKE, J. & WISE, K. 1992. High-frequency network oscillation in the hippocampus. *Science*, 256, 1025-7.
- CANOLTY, R. T., EDWARDS, E., DALAL, S. S., SOLTANI, M., NAGARAJAN, S. S., KIRSCH, H. E., BERGER, M. S., BARBARO, N. M. & KNIGHT, R. T. 2006. High gamma power is phase-locked to theta oscillations in human neocortex. *Science*, 313, 1626-1628.
- CASH, S. S., HALGREN, E., DEHGHANI, N., ROSSETTI, A. O., THESEN, T., WANG, C., DEVINSKY, O., KUZNIECKY, R., DOYLE, W., MADSEN, J. R., BROMFIELD, E., EROSS, L., HALASZ, P., KARMOS, G., CSERCSA, R., WITTNER, L. & ULBERT, I. 2009. The human K-complex represents an isolated cortical down-state. *Science*, 324, 1084-7.
- CONTRERAS, D., TIMOFEEV, I. & STERIADE, M. 1996. Mechanisms of long-lasting hyperpolarizations underlying slow sleep oscillations in cat corticothalamic networks. *The Journal of Physiology*, 494, 251-264.
- DESGRAUPES, B. 2013. Clustering Indices.
- EINEVOLL, G. T., PETTERSEN, K. H., DEVOR, A., ULBERT, I., HALGREN, E. & DALE, A. M. 2007. Laminar population analysis: estimating firing rates and evoked synaptic activity from multielectrode recordings in rat barrel cortex. *Journal of neurophysiology*, 97, 2174-2190.
- FÉVOTTE, C., BERTIN, N. & DURRIEU, J.-L. 2009. Nonnegative matrix factorization with the itakura-saito divergence: With application to music analysis. *Neural Computation*, 21, 793-830.
- GOENSE, J. & LOGOTHETIS, N. K. 2008. Neurophysiology of the BOLD fMRI signal in awake monkeys. *Current Biology*, 18, 631-640.
- HE, B. J., ZEMPEL, J. M., SNYDER, A. Z. & RAICHLE, M. E. 2010. The temporal structures and functional significance of scale-free brain activity. *Neuron*, 66, 353-369.
- HONEY, C. J., KÖTTER, R., BREAKSPEAR, M. & SPORNS, O. 2007. Network structure of cerebral cortex shapes functional connectivity on multiple time scales. *Proceedings of the National Academy of Science USA*, 104, 10240-10245.
- JI, D. Y. & WILSON, M. A. 2007. Coordinated memory replay in the visual cortex and hippocampus during sleep. *Nature Neuroscience*, 10, 100-107.
- LOGOTHETIS, N. K. 2008. What we can do and what we can not do with fMRI. *Nature*, 453, 869-878.
- LOGOTHETIS, N. K., ESCHENKO, O., MURAYAMA, Y., AUGATH, M., STEUDEL, T., EVRARD, H. C., BESSERVE, M. & OELTERMANN, A. 2012. Hippocampal-cortical interaction during periods of subcortical silence. *Nature*, 491, 547-53.
- LOGOTHETIS, N. K., PAULS, J., AUGATH, M., TRINATH, T. & OELTERMANN, A. 2001. Neurophysiological investigation of the basis of the fMRI signal. *Nature*, 412, 150-157.
- LOGOTHETIS, N. K. & WANDELL, B. A. 2004. Interpreting the BOLD signal. *Annu Rev Physiol*, 66, 735-69.
- MAGRI, C., MAZZONI, A., LOGOTHETIS, N. K. & PANZERI, S. 2012. Optimal band separation of extracellular field potentials. *Journal of neuroscience methods*, 210, 66-78.
- MAILHÉ, B., LESAGE, S., GRIBONVAL, R., BIMBOT, F., VANDERGHEYNST, P. & OTHERS. 2008. Shift-invariant dictionary learning for sparse representations: extending K-SVD. 16th European Signal Processing Conference (EUSIPCO'08), 2008 2008.
- MAKAROV, V. A., MAKAROVA, J. & HERRERAS, O. 2010. Disentanglement of local field potential sources by independent component analysis. *Journal of computational neuroscience*, 29, 445-457.

- MARCUS, G., MARBLESTONE, A. & DEAN, T. 2014. Neuroscience. The atoms of neural computation. *Science*, 346, 551-2.
- MITZDORF, U. 1985. Current source-density method and application in cat cerebral cortex: investigation of evoked potentials and EEG phenomena. *Physiol Rev*, 65, 37-100.
- MONTEMURRO, M. A., RASCH, M. J., MURAYAMA, Y., LOGOTHETIS, N. K. & PANZERI, S. 2008. Phase-of-firing coding of natural visual stimuli in primary visual cortex. *Current Biology*, 18, 375-380.
- MURAYAMA, Y., BIE\$MANN, F., MEINECKE, F. C., MÜLLER, K.-R., AUGATH, M., OELTERMANN, A. & LOGOTHETIS, N. K. 2010. Relationship between neural and hemodynamic signals during spontaneous activity studied with temporal kernel CCA. *Magnetic resonance imaging*, 28, 1095-1103.
- NOVIKOV, E., NOVIKOV, A., SHANNAHOFF-KHALSA, D., SCHWARTZ, B. & WRIGHT, J. 1997. Scale-similar activity in the brain. *Phys. Rev. E*, 56, R2387-R2389.
- RAMIREZ-VILLEGAS, J. F., LOGOTHETIS, N. K. & BESSERVE, M. 2015. Diversity of sharp-wave-ripple LFP signatures reveals differentiated brain-wide dynamical events. *Proc Natl Acad Sci U S A*, 112, E6379-87.
- ROBINSON, P. A., RENNIE, C. J. & ROWE, D. L. 2002. Dynamics of large-scale brain activity in normal arousal states and epileptic seizures. *Phys Rev E Stat Nonlin Soft Matter Phys*, 65, 041924.
- ROOPUN, A. K., KRAMER, M. A., CARRACEDO, L. M., KAISER, M., DAVIES, C. H., TRAUB, R. D., KOPELL, N. J. & WHITTINGTON, M. A. 2008. Temporal Interactions between Cortical Rhythms. *Frontiers in Neuroscience*, 2, 145-154.
- ROUSSEEUW, P. J. 1987. Silhouettes: A graphical aid to the interpretation and validation of cluster analysis. *Journal of Computational and Applied Mathematics*, 20, 53-65.
- SCHOMBURG, E. W., FERNÁNDEZ-RUIZ, A., MIZUSEKI, K., BERÉNYI, A., ANASTASSIOU, C. A., KOCH, C. & BUZSÁKI, G. 2014. Theta Phase Segregation of Input-Specific Gamma Patterns in Entorhinal-Hippocampal Networks. *Neuron*.
- SEUNG, D. & LEE, L. 2001. Algorithms for non-negative matrix factorization. *Advances in neural information processing systems*, 13, 556-562.
- SHI, J. & MALIK, J. 2000. Normalized cuts and image segmentation. *Pattern Analysis and Machine Intelligence, IEEE Transactions on*, 22, 888-905.
- SMARAGDIS, P., FEVOTTE, C., MYSORE, G., MOHAMMADIHA, N. & HOFFMAN, M. 2014. Static and Dynamic Source Separation Using Nonnegative Factorizations: A unified view. *Signal Processing Magazine, IEEE*, 31, 66-75.
- SRA, S. & DHILLON, I. S. Generalized nonnegative matrix approximations with Bregman divergences. *Advances in neural information processing systems*, 2005 2005, 283-290.
- THIAGARAJAN, T. C., LEBEDEV, M. A., NICOLELIS, M. A. & PLENZ, D. 2010. Coherence potentials: loss-less, all-or-none network events in the cortex. *PLoS biology*, 8, e1000278-e1000278.
- VARELA, C. 2014. Thalamic neuromodulation and its implications for executive networks. *Front Neural Circuits*, 8, 69.
- WANG, X. J. 2010. Neurophysiological and computational principles of cortical rhythms in cognition. *Physiological reviews*, 90, 1195-268.
- YLINEN, A., BRAGIN, A., NÁDASDY, Z., JANDÓ, G., SZABO, I., SIK, A. & BUZSÁKI, G. 1995. Sharp wave-associated high-frequency oscillation (200 Hz) in the intact hippocampus: network and intracellular mechanisms. *The Journal of neuroscience*, 15, 30-46.

Figures

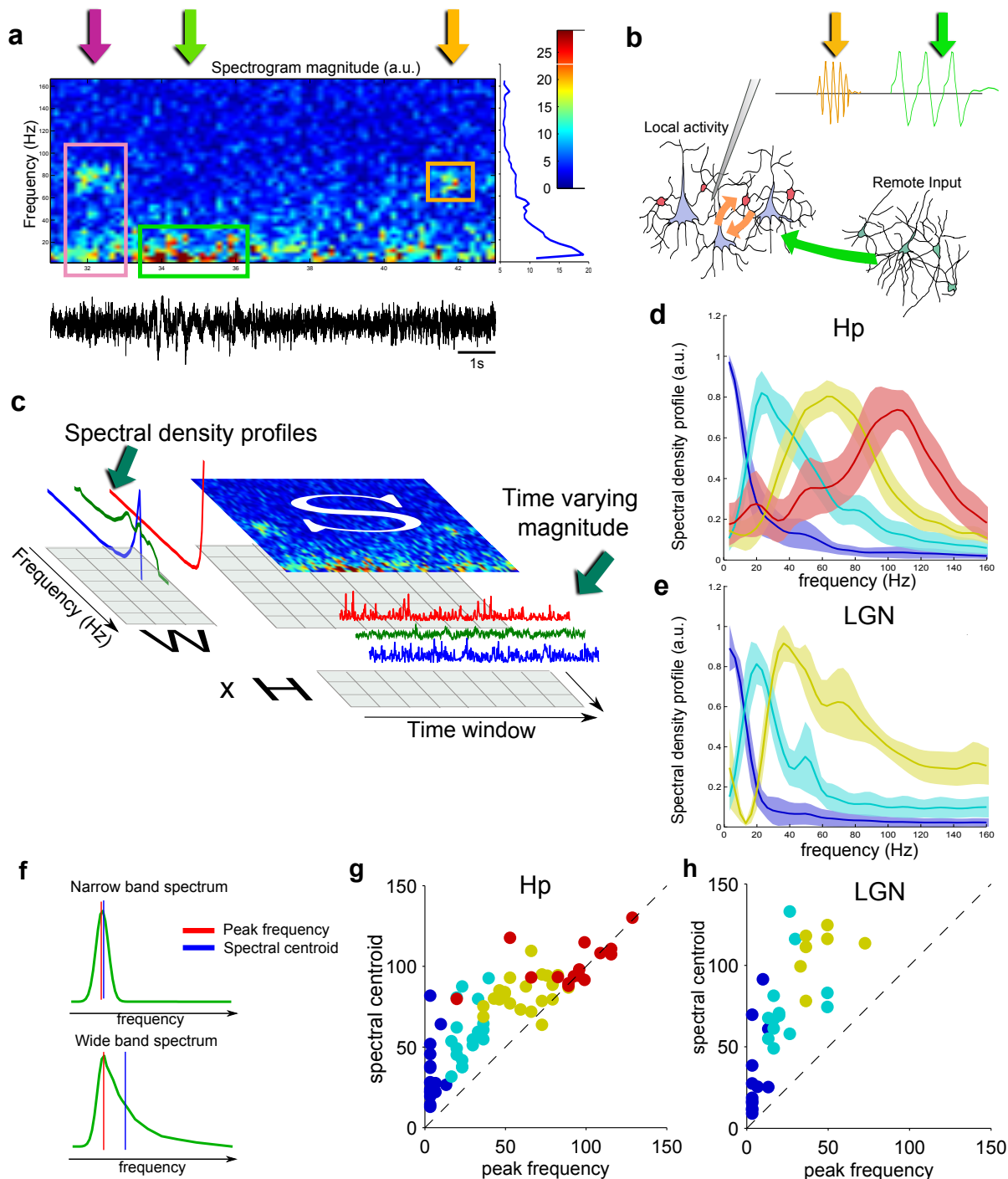


Figure 1: Principle of neural event analysis. (a) Example LFP from the pyramidal layer from monkey CA1 (bottom black trace) and corresponding spectrogram (top) computed with STFT. Rectangles indicate transient spectral power increases, see text. (b) Schematic representation of LFP events (top) and putative underlying neural populations (bottom). Two local groups of neurons, in gray and red interact through recurrent interactions (orange arrows) and receive input (green arrow) from a third population (in green) in a remote brain structure. (c) Principle of NMF applied to the spectrogram matrix \mathbf{S} shown in panel a. \mathbf{S} is approximated by the product of two matrices with non-negative coefficients: \mathbf{W} , gathering the spectral profiles of 3 components, and \mathbf{H} , gathering the time dependent contribution of each component to the LFP spectrogram. (d) Normalized average spectral profiles resulting from the clustering of NMF results for LFP recordings in Hp, area indicates the standard error within each cluster. (e) Same as panel d for LFP recordings in LGN. Additional analysis can be found in Supplementary Fig. 2-3. (f) Schematic representation of two types of power spectral density profiles together with their the location of their peak frequency (in red) and spectral centroid (in blue). (g) Spectral centroid against peak frequency for all hippocampal spectral profiles resulting from NMF analysis. Color indicates cluster membership as in d. (h) Spectral centroid against peak frequency for all LGN spectral profiles cluster. Color indicates cluster membership as in e.

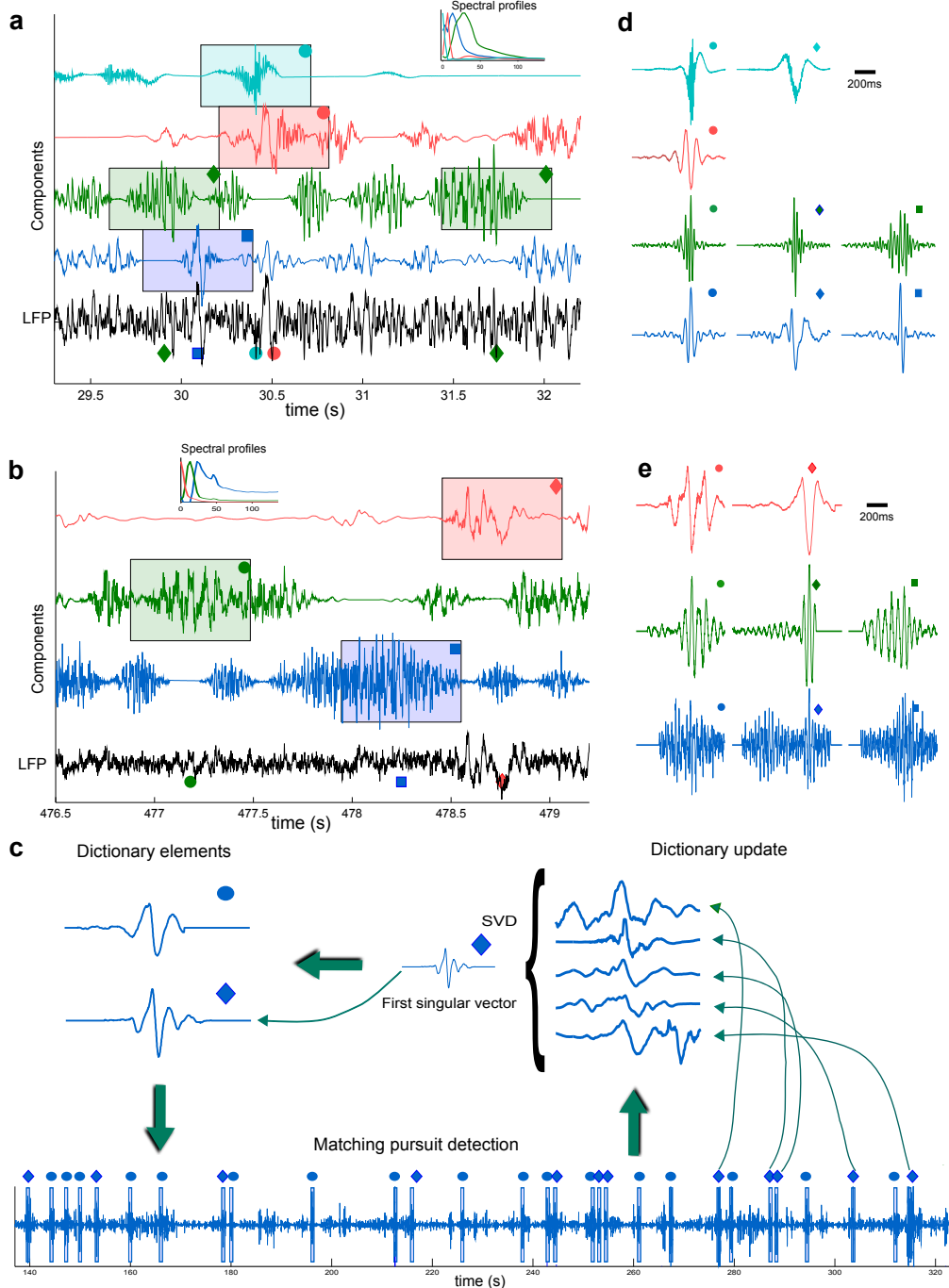


Figure 2: Time course of neural events. (a) Example of dynamical components extracted from CA1 LFP (bottom black trace). Rectangles indicate the location of detected events, the marker in the upper right-hand corner indicates the corresponding dictionary element in panel d. (b) Same as panel a for LFP in LGN. Rectangles indicate the location of detected events, markers indicate dictionary elements in panel e. (c) Principle of shift-invariant dictionary learning. The algorithm alternates between a Matching Pursuit step, which detects the time points where the component time course have maximum similarity with one of the dictionary elements, and an SVD step in which the dictionary patterns are updated using the SVD of the matrix gathering perievent time windows detected during the previous step. (d) Dictionary patterns learned from the dynamical components in panel b. (e) Same as (d) for components in panel c.

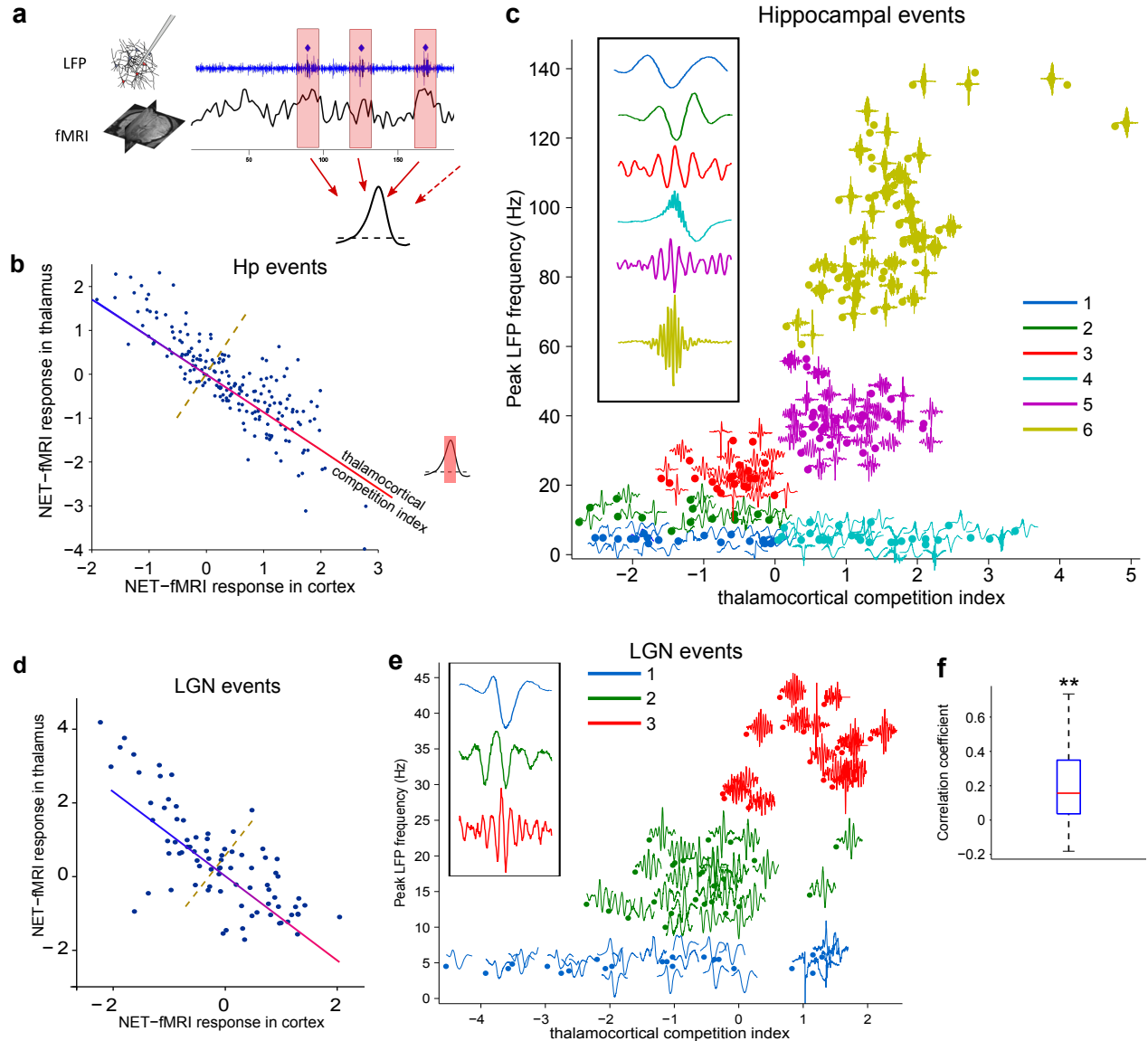


Figure 3: Local versus brain-wide properties of neural events. (a) Schematic representation of the principle of NET-fMRI analysis: the peri-event fMRI traces are averaged across events associated to a given dictionary pattern. (b) Raster plot of the average NET-fMRI response in thalamus and cortex associated to each detected Hp event. As illustrated by the inset, NET-fMRI response is averaged over the interval were it reaches half the maximum response. Correlation between the two variables is significant ($\rho = -.839$, Spearman, $p < 10^{-7}$, $n=171$). The solid line indicates the corresponding fitted linear regression function. (c) Raster plot of the peak frequency of dictionary patterns against thalamocortical competition index (TCI) for Hp events, insets represent magnified examples of dictionary patterns for each cluster. Colors indicates cluster identity. (d) Same as panel b for LGN events. Correlation between the two variables is significant ($(\rho = -.727$, Spearman, $p < 10^{-7}$, $n=80$)). (e) Same as panel c for LGN events. (f) Distribution of correlation coefficient between thalamic and cortical fMRI activity across sessions. (f) Distribution across sessions of average correlation between Thalamic and Cortical fMRI activity. Star indicate significantly positive median (Wilcoxon signed rank test, $p<.01$, $n=20$)

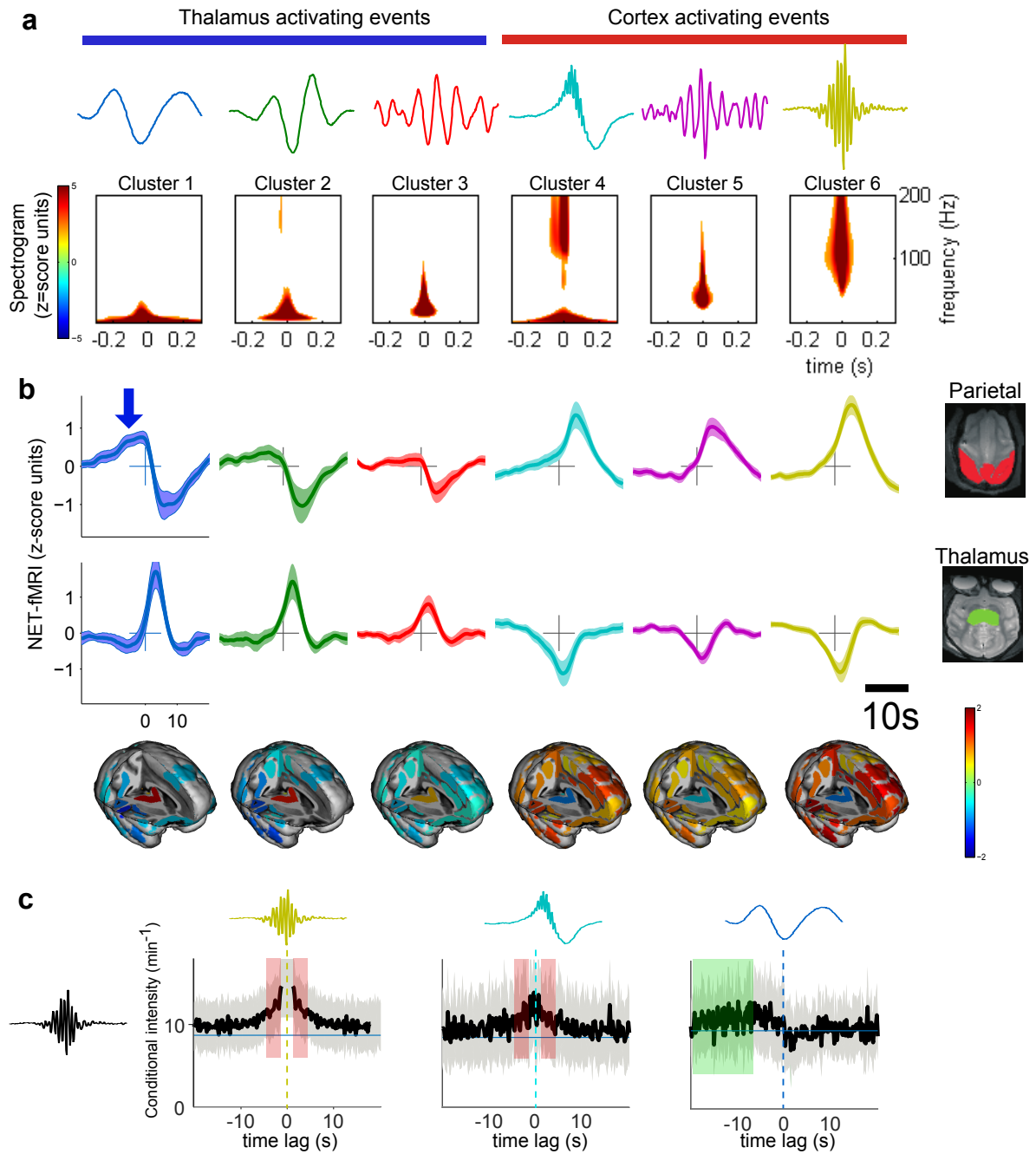


Figure 4: Local and brain-wide physiological properties of hippocampal neural events. (a) Average event triggered time-frequency maps of the 6 clusters of hippocampal events (Z-score with respect to randomized event onsets). Traces at the top represent example dictionary patterns of each cluster. (b) Average NET-fMRI response of the 6 clusters of hippocampal events for selected structures (Z-score with respect to randomized event onsets). Bottom insets represent the trimensional mapping of the amplitude of this response at $t=3\text{s}$ overlaid on a template macaque brain.

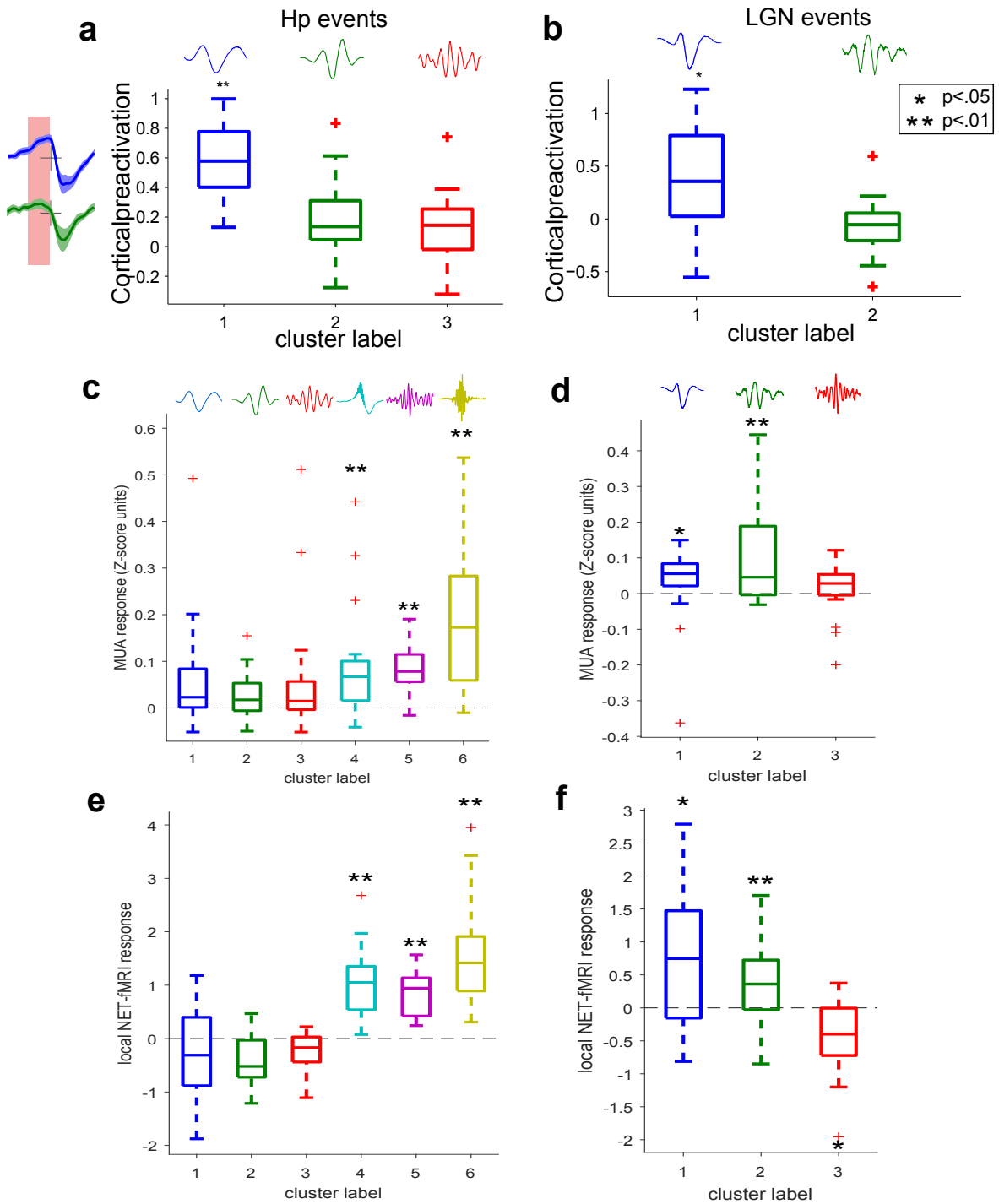


Figure 5: Comparison of LGN and Hp event properties. (a) Distribution of average NET-fMRI response in cortex prior to the event onset (during the pre-activation period, see text) for thalamus activating clusters. Stars indicate significantly positive values (Wilcoxon signed rank test; $p < .01$, Bonferroni corrected, from left to right: $n = 18, 14, 21$). Traces at the top represent example dictionary patterns of each cluster. (b) Same as panel (a) for LGN events. Stars indicate significantly non-zero median values (Wilcoxon signed rank test; $p < .01$, Bonferroni corrected, from left to right: $n = 22, 25$). (c) Distribution of average MUA changes in a 400ms peri-event time window (Z-scored with respect to randomized events) for each Hp event cluster (outliers at 1.23 and .75 for cluster label 4 and .89 for cluster label 6 are out of the axis range). Stars indicate significantly non-zero median values (Wilcoxon signed rank test; $p < .01$, Bonferroni corrected, from left to right: $n = 18, 14, 21, 27, 26, 38$). (d) Same as (c) for LGN events. Stars indicate significantly non-zero median values (Wilcoxon signed rank test; $p < .01$, Bonferroni corrected, from left to right: $n = 22, 25, 16$). (e) Distribution of local (Hippocampal) NET-fMRI changes for each Hp event clusters. (f) Same as (e) for LGN events (NET-fMRI changes in LGN).

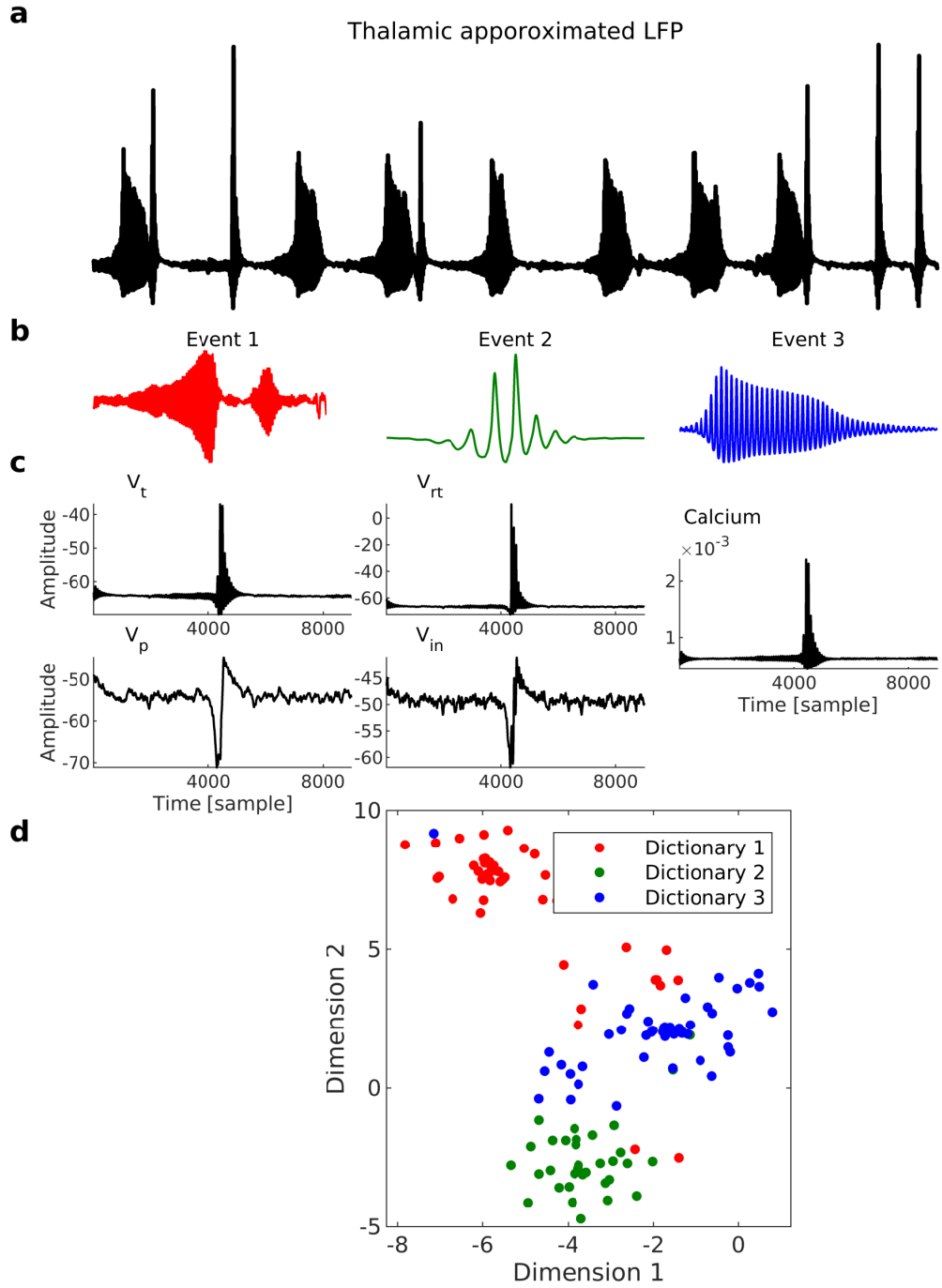


Figure 6: Neural events in a thalamocortical simulation. (a) An exemplary trace for approximated LFP from thalamic module of the thalamocortical simulation. (b) Three Identified events in the approximated LFP. (c) Exemplary trace of cellular variables of the thalamocortical (membrane potential of all 4 populations and the calcium current, see the main text for the details). (d) Representation of cellular dynamics in the vicinity of the identified events (in (b)), in a 2-D subspace (based on tSNE dimensionality reduction). Colors are matching the colors of identified neural events in (b).

The complex spectral structure of transient LFPs reveals subtle aspects of network coordination across scales and structures.

Supplementary information

Michel Besserve^{1,2}, Shervin Safavi¹, Bernhard Schölkopf² and Nikos K. Logothetis^{1,3}

¹Department of Physiology of Cognitive Processes, Max Planck Institute for Biological Cybernetics, Spemannstrasse 38, 72076 Tübingen, Germany.

²Department of Empirical Inference, Max Planck Institute for Intelligent Systems, Spemannstrasse 38, 72076 Tübingen, Germany.

³Centre for Imaging Sciences, Biomedical Imaging Institute, The University of Manchester, Manchester M13 9PT, United Kingdom.

1 Supplementary methods

1.1 Dynamical component decomposition of LFP signals

Using a latent variable model and an associated non-negative matrix factorization (NMF) procedure, it is possible to decompose the single channel LFP time course into a set of dynamical components. We describe in this section the model, the NMF algorithm and the dynamical component estimation.

1.1.1 Gaussian Composite Model

The Gaussian Composite Model (GCM) [Smaragdis et al., 2014] models the input signal $x(t)$ as a mixture of K latent components:

$$X(t) = \sum_{k=1}^K C_k(t).$$

The vector of coefficients of the Short Term Fourier Transform (SFT) of X on a given time window n of length $2T + 1$ centered at time t_n is denoted by:

$$\mathbf{x}_n = (x_{f,n}) = SFT(\{X(t_n + m)\}_{m=-T, \dots, T}).$$

By linearity of the Fourier transform, the mixture can be written in the Fourier domain as:

$$\mathbf{x}_n = \sum_{k=1}^K \mathbf{c}_{n,k}, \quad \mathbf{c}_{n,k} = SFT(\{C_k(t_n + m)\}_{m=-T, \dots, T}).$$

The Fourier coefficients of each component at each non-negative frequency are assumed to be independent normally distributed random variables such that their joint distribution is a multivariate complex Gaussian with a diagonal covariance matrix:

$$\mathbf{c}_{k,n} \sim \mathcal{N}_c(0, h_{k,n} \text{diag}(\mathbf{w}_k)).$$

In this expression, the vector \mathbf{w}_k represents the frequency profile of the power spectral density of component k , while $h_{k,n}$ is the time varying magnitude of component k for window n . In this way, the input signal is modeled as a mixture of several frequency components with a fixed frequency profile and a time varying contribution to each time window.

As a consequence of this Gaussian model, the distribution of Fourier coefficient of the input signal can be expressed by marginalizing the latent components, such that for each frequency f and time window n :

$$x_{f,n} \sim \mathcal{N}_c(0, \sum_k h_{k,n} w_{f,k}).$$

As a consequence, the power spectrogram is exponentially distributed with mean:

$$\overline{s_{f,n}} = \text{var}(x_{f,n}) = \sum_k h_{k,n} w_{f,k} = (\mathbf{W}\mathbf{H})_{f,n},$$

where \mathbf{W} and \mathbf{H} are matrices built from the coefficients $w_{f,k}$ and $h_{k,n}$ respectively.

Given the observed samples of \mathbf{x} , the minus log-likelihood of the two matrices of parameters writes

$$C_{ML}(\mathbf{W}, \mathbf{H}) = - \sum_{f,n} \log \mathcal{N}_c(x_{f,n} \mid 0, \sum_k w_{f,k} h_{n,k}),$$

which can be rewritten up to an additive constant using the Itakura-Saito divergence $d_{IS}(x|y) \hat{=} \frac{x}{y} - \log \frac{x}{y} - 1$:

$$C_{ML}(\mathbf{W}, \mathbf{H}) =_C \sum_{f,n} d_{IS}(|x_{f,n}|^2 \mid \sum_k w_{f,k} h_{n,k}) \hat{=} d_{IS}(\mathbf{S} \mid \mathbf{W}\mathbf{H}).$$

In the last expression, all matrices being non-negative, it appears that finding the maximum likelihood estimates of GCM parameters amounts to solve an approximate non-negative matrix factorization problem with a specific loss: the Itakura-Saito divergence (the divergence for a matrix is defined as the sum of entrywise divergences).

1.1.2 Bregman divergences

The Itakura-Saito divergence is a member of a parametric family of divergences, β -divergences, which are defined for positive scalars x and y as:

$$d_\beta(x|y) = \begin{cases} \frac{1}{\beta(\beta-1)}(x^\beta + (\beta-1)y^\beta - \beta xy^{\beta-1}) & \beta \in \mathbb{R} \setminus \{0, 1\} \\ x \log\left(\frac{x}{y}\right) + (y-x) & \beta = 1 \\ \frac{x}{y} - \log\left(\frac{x}{y}\right) - 1 & \beta = 0 \end{cases}$$

Interestingly, this family includes the squared Euclidean norm ($\beta = 2$), the Kullback–Leibler divergence (1), and the Itakura-Saito divergence ($\beta = 0$) as special cases. The non-negative factorization problem can be addressed for any of these divergences in a common framework explained in the next section. One property specific to the Itakura-Saito divergence is scale invariance: assume variables x and y are rescaled by a multiplicative positive factor s , it immediately follows from the definition that $d_{IS}(sx|sy) = d_{IS}(x|y)$. As a consequence, Itakura-Saito NMF is invariant to rescaling of the lines of the spectrogram matrix \mathbf{S} associated to each frequency.

1.1.3 Non-negative matrix factorization

The non-negative factorization problem for a given Bregman divergence d_β can be written as:

$$\min_{\mathbf{W} \geq 0, \mathbf{H} \geq 0} d_\beta(\mathbf{S}|\mathbf{WH}).$$

The minimum of this objective is reached at a stationary point, which satisfies the Karush-Kuhn-Tucker (KKT) optimality conditions:

$$\mathbf{W} \odot \nabla_{\mathbf{W}} d_\beta(\mathbf{S}|\mathbf{WH}) = 0 \text{ and } \mathbf{H} \odot \nabla_{\mathbf{H}} d_\beta(\mathbf{S}|\mathbf{WH}) = 0.$$

Computing the expression of the gradient $\nabla_{\mathbf{W}} d_\beta(\mathbf{V}|\mathbf{WH})$, we get for the first KKT condition:

$$\mathbf{W} \odot (\mathbf{W}^T (\mathbf{S} \odot (\mathbf{WH})^{\beta-2})) = \mathbf{W} \odot (\mathbf{W}^T (\mathbf{WH})^{\beta-1}).$$

and an equivalent expression in \mathbf{H} for the second KKT condition.

The multiplicative update algorithm proposes to search for a stationary point satisfying this condition by using the fixed point iteration:

$$\mathbf{W}_{k+1} = \mathbf{W}_k \odot \frac{(\mathbf{S} \odot (\mathbf{WH})_k^{\beta-2}) \mathbf{H}_k^T}{(\mathbf{WH})_k^{\beta-1} \mathbf{H}_k^T}.$$

We can easily verify from this last equation that if the algorithm reaches a stationary point, the above KKT conditions are satisfied.

1.1.4 Bootstrapping and stabilization of NMF solution

While NMF is an appropriate technique for our problem, we observed that the convergence of the algorithm can be sensitive to initialization. There is no guaranty of convergence to the global optimum of the objective since it is not convex. To ensure robust convergence of the algorithm to a stable solution, we design a bootstrap technique that iteratively stabilizes the solution. The procedure follows three steps: initialization, bootstrap and final optimization described in the next paragraphs.

Initialization At the beginning, all elements of the matrix \mathbf{W} are drawn independently from a uniform distribution on the interval $[0, 1]$:

$$(\mathbf{W}_{init})_{ij} \sim \mathcal{U}(0, 1).$$

The matrix \mathbf{H} is then initialized accordingly using least-square linear regression of the matrix \mathbf{S} by solving:

$$\tilde{\mathbf{H}} = \arg \min_{\mathbf{H}} \|\mathbf{S} - \mathbf{W}_{init}\mathbf{H}\|^2.$$

Since the solution of this minimization problem is not guaranteed to be non-negative, we take the positive part of each entry to build the initialization matrix (negative entries are zeroed), we write this operation as:

$$\mathbf{H}_{init} = (\tilde{\mathbf{H}})^+.$$

Bootstrap We run 50 bootstrap iterations as follows. Starting from the initialized matrices, we partition the N columns of the matrix \mathbf{S} in two subsets of equal length by random permutation of the columns, the $N/2$ first columns being assigned to the first subset and the last to the second.

The NMF optimization is then run separately on the two matrices built from the columns of the respective subsets resulting in two solutions: $(\mathbf{W}_1, \mathbf{H}_1)$ and $(\mathbf{W}_2, \mathbf{H}_2)$. While the matrices \mathbf{H}_1 and \mathbf{H}_2 are not related, the columns of \mathbf{W}_1 and \mathbf{W}_2 should in principle reach similar values assuming the number of samples is large enough and the solution of the NMF being stable for this number of components. However, the similarity between columns is up to a permutation of the components. We thus assess similarity by first reordering the columns so that they match together. The ordering of the components is done by computing the kernel PCA of all columns of both matrices pooled together. Then the components of each sub-matrix are reordered according to the value of their projection on the first PCA component.

Once the components are reordered, pairs of columns from each matrix are matched together according to this order and a similarity measure between them is computed according to their mean absolute log ratio. For pairs exceeding the similarity threshold of .1, the corresponding columns are kept for the initialization of the next bootstrap iteration, while the remaining columns will simply be initialized again as described in the previous subsection.

Final optimization After 50 bootstrap iterations, the spectral components found in the last 5 iterations are averaged together to build the final initialization matrix \mathbf{W} , and the NMF algorithm is run on the full matrix \mathbf{S} to provide the final solution.

1.1.5 Wiener filtering

Under the GCM assumption, once the matrix parameters \mathbf{H} and \mathbf{W} have been estimated using IS-NMF, it is possible to estimate the time course of the latent components. Taking the example of the first component, estimating $C_1(t)$ from data $X(t)$ amounts to denoising the input signal corrupted by an additive noise $\eta(t)$ which is the sum of all other latent components:

$$X(t) = C_1(t) + \eta(t), \quad \eta(t) = C_2(t) + \dots + C_K(t).$$

On each time window n , components are stationary Gaussian time series fully specified by the matrix \mathbf{W} and the n^{th} column of \mathbf{H} , $\mathbf{H}_{.n}$ and the optimal reconstruction of source signal associated to component k in the Fourier domain is given by the generalized Wiener filter [Smaragdis et al., 2014]

$$\hat{\mathbf{c}}_{nk} = (\mathbf{W}_{.k} \mathbf{H}_{kn}) \oslash (\mathbf{W} \mathbf{H}_{.n}) \odot \mathbf{x}_n,$$

where \odot denotes the entrywise product and \oslash the entrywise division. The resulting estimated time course $\hat{C}_k(t)$ on time frame n can be calculated by inverse Fourier transform of $\hat{\mathbf{c}}_{nk}$. An intuitive interpretation of this procedure in the time domain is that the components correspond to the output of a time varying filter bank, the transfer function \mathbf{f}_{kn} of each filter k and time frame n being given by

$$\mathbf{f}_{kn} = (\mathbf{W}_{.k} \mathbf{H}_{kn}) \oslash (\mathbf{W} \mathbf{H}_{.n}),$$

and thus correspond to a normalized version of the original spectral density $\mathbf{W}_{.k}$ of each component.

1.2 Event detection

1.2.1 Shift-invariant dictionary learning

The objective of dictionary learning is to find a sparse representation of a signal using a set of basis functions. While several sparse representations use predefined basis functions, such as wavelets, dictionary learning also learns these functions from data, in order to achieve a better representation. Among classical dictionary learning techniques, KSVD has become a reference, both for its simplicity and efficiency on real data [Aharon et al., 2006]. KSVD relies on applying two steps iteratively: orthogonal matching pursuit, which learns a sparse representation for a fixed set of basis functions, and a dictionary improvement step, which is implemented efficiently using Singular Value Decomposition (SVD). The analysis of long time series such as ongoing brain activity poses an additional challenge, since the interesting patterns in these time series can be present at multiple times that are unknown a priori. Classical dictionary learning techniques such as KSVD reveal inefficient since they need to learn a large dictionary containing similar instances with different time lags. In contrast, shift invariant dictionary learning approaches address this issue by learning fixed dictionary patterns (also named *atoms* in the literature) and adjust an additional time lag parameter to fit each possible occurrence of these patterns. An efficient shift invariant generalization of KSVD to long time series was proposed by [Mailhé et al., 2008] in the context of music analysis.

Here we implemented a modified version adapted to our specific application. To prevent overlap between neural events, we impose to the dictionary to capture the time course of the ongoing activity with at most one pattern at a time. In this way, the detected patterns correspond directly to segments of the dynamical component under analysis. In addition to this modification, we developed a cross-validation methodology to estimate the parameters of the dictionary on empirical data, described in the next section.

1.2.2 Selection of the number of events and patterns

For a fixed number of dictionary patterns, we use a cross-validation procedure to find the optimal number of events. To focus on events frequent enough to assess their properties statistically, but rare enough such that their NET-fMRI response can be isolated, we assume each type of event to have a rate of occurrence ranging from 2 per minute to 12 per minute and tested 6 possible rates between these values (2, 4, 6, 8, 10 and 12 events per minute). For a given rate, we fixed the number of events of the shift invariant dictionary learning algorithm according to the length of the recording. After running the algorithm, the detected events were removed from the original time series, and added again to it at random times. We then run the algorithm a second time and evaluate how many of these new events were detected during this new run. We then chose the number of events achieving the best average performance in the retrieval of the randomized events. The number of patterns was initialized to 3, and then decreased as long as the proportion of events associated to each pattern stays above a minimum value (to enforce the method to focus on frequent patterns). The minimum proportion was set to be 50% of the proportion achieved by a equipopulated repartition of the events among the different patterns. This minimum proportion thus corresponds to 15% and 25% for 2 and 3 patterns respectively. If this minimum proportion is not achieved, the number of patterns is ultimately reduced to 1. The performance of this selection procedure is studied in the supplementary results section.

1.3 Characterization of spectral profiles

1.3.1 Spectral centroid and spectral purity ratio

Beyond comparing peak frequencies of spectral profiles, assessing whether the detected spectral components reflect pure narrow-band oscillations (i.e. with a power spectral density having a single narrow peak) or more complex dynamical patterns is important to understand the underlying neural mechanisms. In particular, the non-linear properties of the underlying network interactions can affect the shape of the Power Spectral Density (PSD) of the observed neural time series, for example by generating harmonics at multiples of the peak frequency [Abey suriya et al., 2014]. To quantify this, we evaluated the spectral centroid of each spectral component. Let $\mathbf{S}(f)$ be the PSD of a given discrete signal, the spectral centroid is the center of mass of this distribution in the frequency domain, defined as:

$$c(\mathbf{S}) = \frac{\int_0^{1/2} f\mathbf{S}(f)df}{\int_0^{1/2} \mathbf{S}(f)df}.$$

As schematized on Figure 1f in main text, for a narrow-band oscillation, the spectral centroid matches very closely the peak frequency. In contrast, discrepancies between the spectral centroid and the peak frequency reveals that the energy is not well concentrated around the peak of the power spectrum, and thus indicates that the signal is not well approximated by a sinusoidal rhythm. As a consequence, we define the *spectral purity ratio* as the ratio of the spectral centroid to the peak frequency. A spectral purity ratio differing from one (or a non-zero log spectral purity ratio) thus indicates that the observed signal differs from a sinusoid and possibly reflects non-linear network interactions.

1.3.2 Illustration with wavelets

To further illustrate how the discrepancy between spectral centroid and peak frequency mark a non-sinusoidal time course, we show how these peak frequency and spectral centroid are related for example to transient patterns originating from wavelet theory [Mallat, 1999]. Since the invention of wavelet analysis, multiple types of wavelets have been designed with various properties for modeling transient signals. Among them, the Morlet wavelet exhibits the closest similarity to short lived sinusoidal oscillation. Alternatively, coiflets show sharp changes in their time course that distinguish them from a sinusoidal pattern. Supplementary Fig. 3b illustrates the time course of these wavelets and show the corresponding absolute value of their Fourier transform. While the Morlet wavelet exhibits a single peak in the Fourier domain, the coiflet shows multiple peaks with decreasing amplitude as the frequency increases. When combining multiple coiflets with different time scales, as illustrated in Supplementary Fig. 3 with two coiflets, the frequency content becomes closer to the monotonously decreasing profiles as observed in our empirical results in Figure 1d-e. From the squared Fourier transform of the wavelet patterns, we derive the same spectral peaks and centroid parameters as for our empirical results. The spectral purity ratio is .98 for the Morlet wavelet and 1.16 for the coiflet, showing non-sinusoidal wavelets exhibit larger discrepancy between these two parameters. When combining two coiflets with different scales, this ratio reached 2.6. In sum, these illustrative examples show the spectral profiles provided by the IS-NMF approach can be characterized beyond the classical peak frequency property to reflect more subtle properties of the time course of neural activity.

1.4 Analysis of thalamocortical model

1.4.1 Biophysical simulation of thalamocortical system

In order to investigate to what degree the detected neural events are informative about the cellular processes such as dynamics of the membrane potentials and ionic currents we exploit a simulation of thalamocortical system developed by Costa et al. [2016]. As the details of the model are described earlier [Costa et al., 2016], we restrict ourselves to a brief explanation of the model.

The model of Costa et al. [2016] is a conductance-based neural mass model [Robinson et al., 1997, Liley et al., 1999, 2002, Wilson et al., 2006]. In this class of neural models, population activity can be approximated by the mean membrane potentials, based on an empirical firing rate function [Marreiros et al., 2008]. Populations interact with each other through the synapses. The spike rate of a sender pre-synaptic population elicits a post-synaptic response in a receiving population and the dynamics of this post-synaptic response is determined by a convolution involving the conventional alpha function for synapses.

This thalamocortical neural mass model is consist of 2 modules, a thalamic and a cortical module. The architecture of each module is adopted from Weigenand et al. [2014]. Briefly each of the two modules consist of two sub-module, one excitatory and one inhibitory population. Both excitatory sub-modules of the model are reciprocally connected to both excitatory and inhibitory population of the other module. Furthermore, all sub-modules receive independent background noise in addition to what they recieve through synaptic interaction with other populations.

The thalamic module is consist of a excitatory sub-module, thalamocortical population (t), and an inhibitory sub-module, reticular (r) population. These sub-modules are connected

via AMPA and GABA synapses, but with different synaptic time constant and only the inhibitory population (reticular) has self-connection. Furthermore, in the thalamic module, various ionic currents has been incorporated for the realistic genesis of spindle oscillations. These currents consist of potassium leak current, T-type calcium currents and an rectifier current.

The cortex module similarly consist of an excitatory sub-module, population of pyramidal neurons (p), and an inhibitory sub-module, population of interneurons (i) and similar to thalamic module, they are connected via AMPA and GABA synapses. In contrast to thalamic module, in the cortex module, both sub-modules have self-connections. Furthermore, in the cortex module, some adaptation mechanisms for firing rates has been incorporated which is necessary for transitioning to down (silent) state.

1.4.2 Event detection in the thalamocortical model

Neural events in the thalamocortical model was identified with the similar procedure used for neural data. As the extracellular field potential stems mainly from activity of pyramidal neurons [Buzsaki et al., 2012], we used the membrane potential of pyramidal neurons in thalamus module as a crude proxy of thalamus LFP and identify the neural events in the time course of the signal. First the short-term Fourier transform (STFT) of the signals over overlapping time windows was computed, then by applying non-negative matrix factorization (NMF) on the spectrograms results from STFT of the LFP, we identify the spectral profile of the characteristic transients of LFP. Lastly, by applying shift-invariant dictionary learning we temporally localize the neural events and identify their sub-types. The number of component chosen for NMF factorization was 3, based on the procedure explain in the method section of the main text.

1.4.3 Low dimensional representation of cellular dynamics

We represent the cellular dynamics during the occurrence of the events in a 2-dimensional (after dimensionality reduction) sub-space. We consider the full space span by concatenated time course of all membrane potentials and the calcium current. Membrane potentials were consist of cortex pyramidal and inhibitory population, and thalamic reticular and thalamocortical (excitatory) populations. Around each event, a window of length 1000 sample has been used for the time course of each cellular variable. To represent cellular dynamics in low dimentional sub-space we used t-distributed stochastic neighbor embedding (tSNE) [van der Maaten and Hinton, 2008].

2 Supplementary results

2.1 Comparison of NMF techniques

We run a comparison of NMF techniques to address the problem of identifying events with different spectral profiles occurring in a time series. Events were generated by bandpass filtering three homogenous Poisson processes in different frequency bands (5Hz, 20Hz and 50Hz respectively) with impulse responses of differing amplitude (1, .5 and .1 respectively). As a consequence (see example time course in Supplementary Fig. 1a), the high frequency events have less energy than the low frequency events, as frequently observed in empirical

LFP time series. The spectral profiles corresponding to each processes are represented in Supplementary Fig. 1b. The three filtered process are then summed and a small Gaussian white noise (with standard deviation .001) added to generate the input time series. To retrieve the three spectral profiles from this mixture signal, we used two NMF approaches: Euclidean NMF and IS-NMF using 4 components (one extra components is used to capture the noise). The similarity between original and retrieved spectral profiles was quantified using cosine similarity. The average performance on each approach is reported in Supplementary Fig. 1c. While both approaches perform well for low and middle frequency profiles (reaching the maximal cosine similarity value 1), only IS-NMF reliably estimates the high frequency profile.

2.2 Dictionary learning

To check the validity of our dictionary learning approach, we simulated noisy time series with different neural events occurring across time. To measure time related quantities in seconds, we assumed a sampling rate of 500Hz. Events were generated by bandpass filtering unit amplitude impulses from an homogenous Poisson process from which we excluded overlapping events by eliminating any event occurring less than 1s after a previous one. To replicate the setting reported in the main text, in which each dynamical component is analyzed separately with this approach, the time course of the generated neural events are chosen in order to have similar frequency properties but possibly different time courses that indicate different subtypes of events. This was done by choosing Butterworth band pass filters with a common center frequency of 5Hz but different bandwidth (.89 and 4.47Hz respectively). Twenty simulations were performed for two cases: either only one or both of these subtypes of events are generated in the time series (which means the dictionary had either one or two patterns), allowing us to assess whether our approach retrieves correctly the number of event subtypes present in the data. An example simulated time series is shown in Supplementary Fig. 5a, with a magnified portion showing the two types of simulated events present in this data (Supplementary Fig. 5b), the most oscillatory events being generated by the band-pass filters with the smallest band-width. We applied the dictionary learning approach as described in Supplementary Methods in order to learn the different types of events and detect their occurrence. The approach was implemented assuming a maximum number of dictionary patterns of 3, and the number of events was selected from an equispaced grid of 8 values ranging from 66 to 400. The dictionary patterns learned from the data of Supplementary Fig. 5a is shown on panel c of the same Figure, witnessing that the shape and number of event subtypes is well recovered. We assessed quantitatively the performance of our approach by first quantifying whether the total number of generated events was correctly estimated. Supplementary Fig. 5d shows the original distribution of the number of events in the simulation, while the corresponding estimated number of events is shown in Supplementary Fig. 5e. This shows the estimated number of events is close to the original value in most cases. Moreover, the correct number of event subtypes is correctly estimated in 80% of the cases (Supplementary Fig. 5(f)).

2.3 Comparison of Hp and LGN events

According to the similarities shown in the two dimensional maps of event properties in Figure 4c and 4e, we compared Hp Cluster 1 to LGN Cluster1, Hp Cluster 2 and 3 to LGN

Cluster 2, and Hp Cluster 4 to LGN Cluster 3. By first comparing their peak frequency (Supplementary Fig. 7a), we found the that lower frequency Hp and LGN events (labeled Cluster 1 in both cases) were comparable in this respect, so as well as gamma band events (Hp Cluster 5 and LGN Cluster 3). On the contrary, neither HP Cluster 2 nor 3 were matching the higher frequency TA LGN Cluster 2 as far as their peak frequency is concerned. In addition to differences in peak frequencies, LFP dynamics of neural events can be compared according to finer properties of the Fourier transform of their associated dictionary patterns. In particular, we can extend the analysis of spectral purity ratio performed on the NMF spectral profiles in a previous section to assess how close to a sinusoid are each event by computing the log of the spectral purity ratio, which should be close to zero for nearly sinusoidal events. Comparison of the log spectral purity ratio between Hp and LGN events (Supplementary Fig. 7b) shows that the two lower frequency TA events from each structure (Clusters 1 and 2 in each structure) are comparable. On the contrary the TA Hp cluster of highest frequency (Cluster 3) has significantly lower spectral purity ratio. In the same way, in the low gamma band, Hp events have lower spectral purity ratio than their LGN counterpart. These results are in accordance with the our analysis of spectral profiles, suggesting a larger contribution of non-linear network interactions in LGN high frequency events than in Hp events of comparable frequency.

3 Supplementary discussion

Time frequency decomposition

Our methodology is based on short-term Fourier transform (SFFT) of the LFP signals over overlapping time windows. Other types of time-frequency decompositions [Martin and Flandrin, 1985, Rioul and Vetterli, 1991] (wavelet transform, Wigner-Ville distribution) could possibly be used and possibly generalize the present approach. However, SFFT provides a much faster time frequency representation of the signal, together with a sound statistical modeling framework [Smaragdis et al., 2014]. As a consequence, while the SFFT representation shown at the beginning of the paper might look noisier than other time frequency representation, it actually carries all necessary statistical information to lead to a decomposition of the LFP time course into a sum of dynamical components. As opposed to a classical time-frequency representation, our approach thus offers a direct visualization of the time courses of different dynamical aspects of the LFP, instead of an abstract representation through wavelet coefficients or spectrograms with a lower time resolution.

Dictionary learning

To analyze quantitatively the interesting patterns that could, to some extent, be readily visually identified in this decomposition, we performed a detailed quantitative analysis of dynamical events by learning a dictionary of recurrent dynamical patterns for each component. This approach enables to isolate different dynamical events that might not be easily identifiable from their power spectral density, as illustrated by sharp-waves (cortex-activating) and low-frequency thalamus-activating events in the hippocampus. Dictionary learning can also be related to wavelet analysis techniques used for example to provide a sparse description of a signal in classical matching pursuit [Mallat and Zhang, 1993]. Our approach indeed provides

a fully automated optimization of a sparse representation with a few dictionary patterns, while in wavelet analysis the shape of those patterns is strongly constrained by a fixed set of basis functions, which has to be selected first. While in principle, dictionary learning could be applied directly to the original LFP time course, the NMF based decomposition is critical for reducing the complexity of the time series such that even dynamical patterns with low energy can be robustly detected.

Generality of the approach

Our approach is a fully unsupervised technique: no additional information (such as behavior or sensory input) is required to assess relevant frequency bands, in contrast to other methods [Magri et al., 2012]. As a consequence our approach is particularly well suited to study ongoing activity in various passive or active states and enables a precise study of the evolution of the dynamical content of neural activity from sleep and anesthesia to cognition and complex behavior. Although our approach does not use any prior knowledge on the structure under study, it was able to retrieve the known characteristic events of both structures during passive states, namely delta oscillation, and spindles for thalamus, and shape-wave ripples and gamma oscillations for hippocampus. This supports that the assumptions underlying our method are general enough to capture a wide range of dynamical events without any tuning from the experimenter, and shows for the first time a description of these activity that is not biased by human expertise. Along this line, we noticed that many of our detected waveforms were more complex than quasi-sinusoidal oscillations. Analysis of the power law behavior of broad band LFP power spectrum has previously been suggested to quantify scale free properties and self-similarity in these time series and was proposed as a model of arrhythmic brain activity that can be taken apart from quasi-sinusoidal components [He et al., 2010]. While our results suggest that many interesting neural events are not quasi-sinusoidal, whether they are related to self-similar processes is an interesting future direction. In addition, we stress that this approach can be applied to single channel data (while generalization to multiple channels will be addressed in future work) because it does not rely on assumptions on the spatial spread of the activity due to multiple underlying current generators. The activity captured in each component may or may not reflect spatially segregated generators; in particular, a same generator can contribute to different components at different times if it is involved in different dynamical network events. The spatial characteristics of each components or events can however be further studied in the context of multiple channel recordings and/or concurrent recording of brain wide activity with neuroimaging techniques.

References

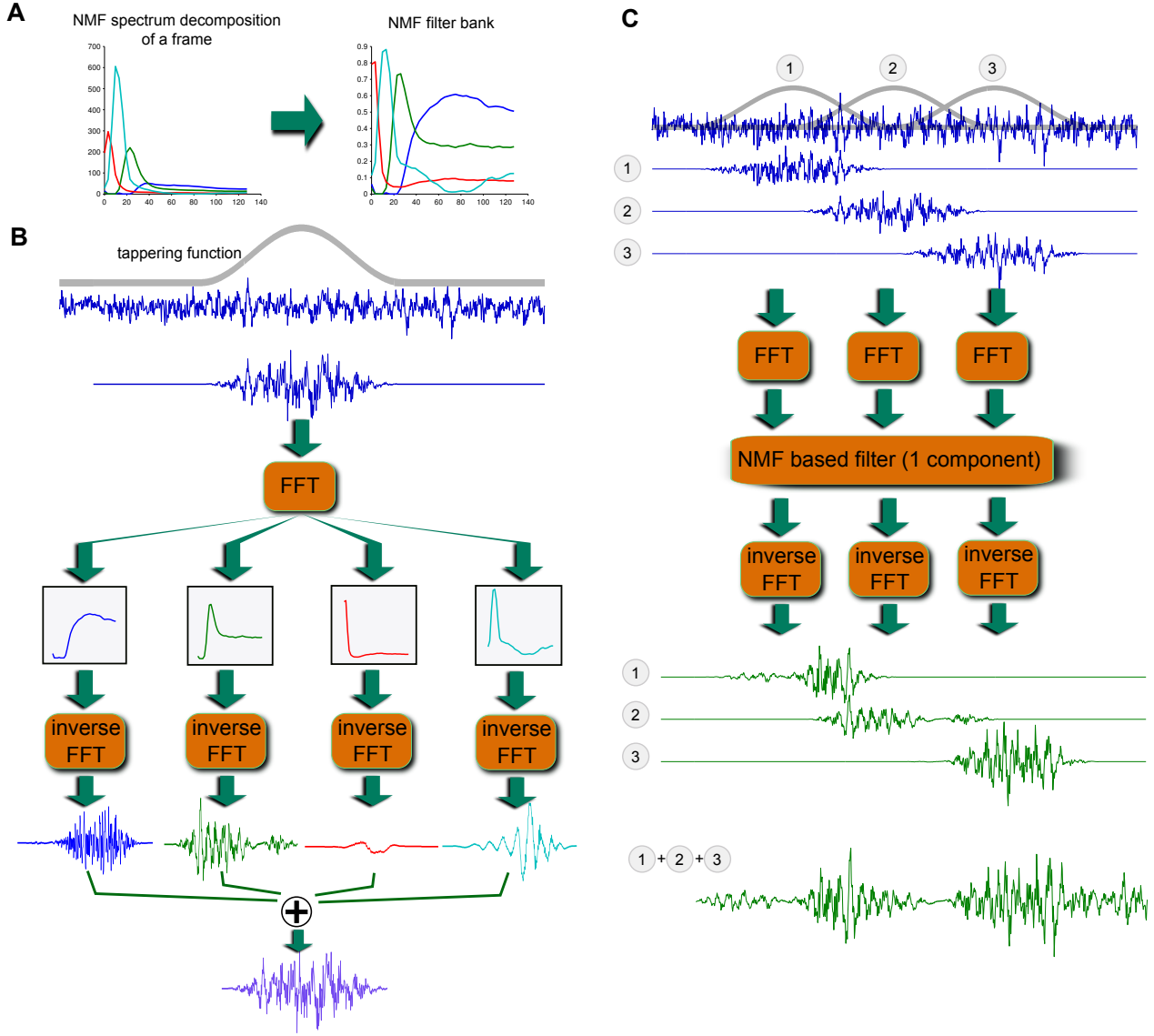
- R. G. Abeysuriya, C. J. Rennie, and P. A. Robinson. Prediction and verification of nonlinear sleep spindle harmonic oscillations. *Journal of Theoretical Biology*, 344:70–77, Mar. 2014. ISSN 0022-5193. doi: 10.1016/j.jtbi.2013.11.013.
- M. Aharon, M. Elad, and A. Bruckstein. -svd: An algorithm for designing overcomplete dictionaries for sparse representation. *Signal Processing, IEEE Transactions on*, 54(11): 4311–4322, 2006.

- G. Buzsaki, C. A. Anastassiou, and C. Koch. The origin of extracellular fields and currents—EEG, ECoG, LFP and spikes. *Nature reviews. Neuroscience*, 13(6):407–20, May 2012. ISSN 1471-0048 (Electronic) 1471-003X (Linking). doi: 10.1038/nrn3241.
- M. S. Costa, A. Weigenand, H.-V. V. Ngo, L. Marshall, J. Born, T. Martinetz, and J. C. Claussen. A Thalamocortical Neural Mass Model of the EEG during NREM Sleep and Its Response to Auditory Stimulation. *PLOS Computational Biology*, 12(9):e1005022, Sept. 2016. ISSN 1553-7358. doi: 10.1371/journal.pcbi.1005022.
- B. J. He, J. M. Zempel, A. Z. Snyder, and M. E. Raichle. The temporal structures and functional significance of scale-free brain activity. *Neuron*, 66(3):353–369, 2010.
- D. T. J. Liley, P. J. Cadusch, and J. J. Wright. A continuum theory of electro-cortical activity. *Neurocomputing*, 26–27:795–800, June 1999. ISSN 0925-2312. doi: 10.1016/S0925-2312(98)00149-0.
- D. T. J. Liley, P. J. Cadusch, and M. P. Dafilis. A spatially continuous mean field theory of electrocortical activity. *Network*, 13(1):67–113, Jan. 2002. ISSN 0954-898X. doi: 10.1088/0954-898X/13/1/303.
- C. Magri, A. Mazzoni, N. K. Logothetis, and S. Panzeri. Optimal band separation of extracellular field potentials. *Journal of neuroscience methods*, 210(1):66–78, 2012.
- B. Mailhé, S. Lesage, R. Gribonval, F. Bimbot, P. Vandergheynst, et al. Shift-invariant dictionary learning for sparse representations: extending k-svd. In *16th European Signal Processing Conference (EUSIPCO'08)*, 2008.
- S. G. Mallat. *A Wavelet Tour of Signal Processing*. Academic Press, San Diego, 2nd ed edition, 1999. ISBN 978-0-12-466606-1.
- S. G. Mallat and Z. Zhang. Matching pursuits with time-frequency dictionaries. *Signal Processing, IEEE Transactions on*, 41(12):3397–3415, 1993.
- A. C. Marreiros, J. Daunizeau, S. J. Kiebel, and K. J. Friston. Population dynamics: Variance and the sigmoid activation function. *NeuroImage*, 42(1):147–157, Aug. 2008. ISSN 1053-8119. doi: 10.1016/j.neuroimage.2008.04.239.
- W. Martin and P. Flandrin. Wigner-ville spectral analysis of nonstationary processes. *Acoustics, Speech and Signal Processing, IEEE Transactions on*, 33(6):1461–1470, 1985.
- O. Rioul and M. Vetterli. Wavelets and signal processing. *IEEE signal processing magazine*, 8(LCAV-ARTICLE-1991-005):14–38, 1991.
- P. A. Robinson, C. J. Rennie, and J. J. Wright. Propagation and stability of waves of electrical activity in the cerebral cortex. *Phys. Rev. E*, 56(1):826–840, July 1997. doi: 10.1103/PhysRevE.56.826.
- P. Smaragdis, C. Fevotte, G. Mysore, N. Mohammadiha, and M. Hoffman. Static and dynamic source separation using nonnegative factorizations: A unified view. *Signal Processing Magazine, IEEE*, 31(3):66–75, 2014.

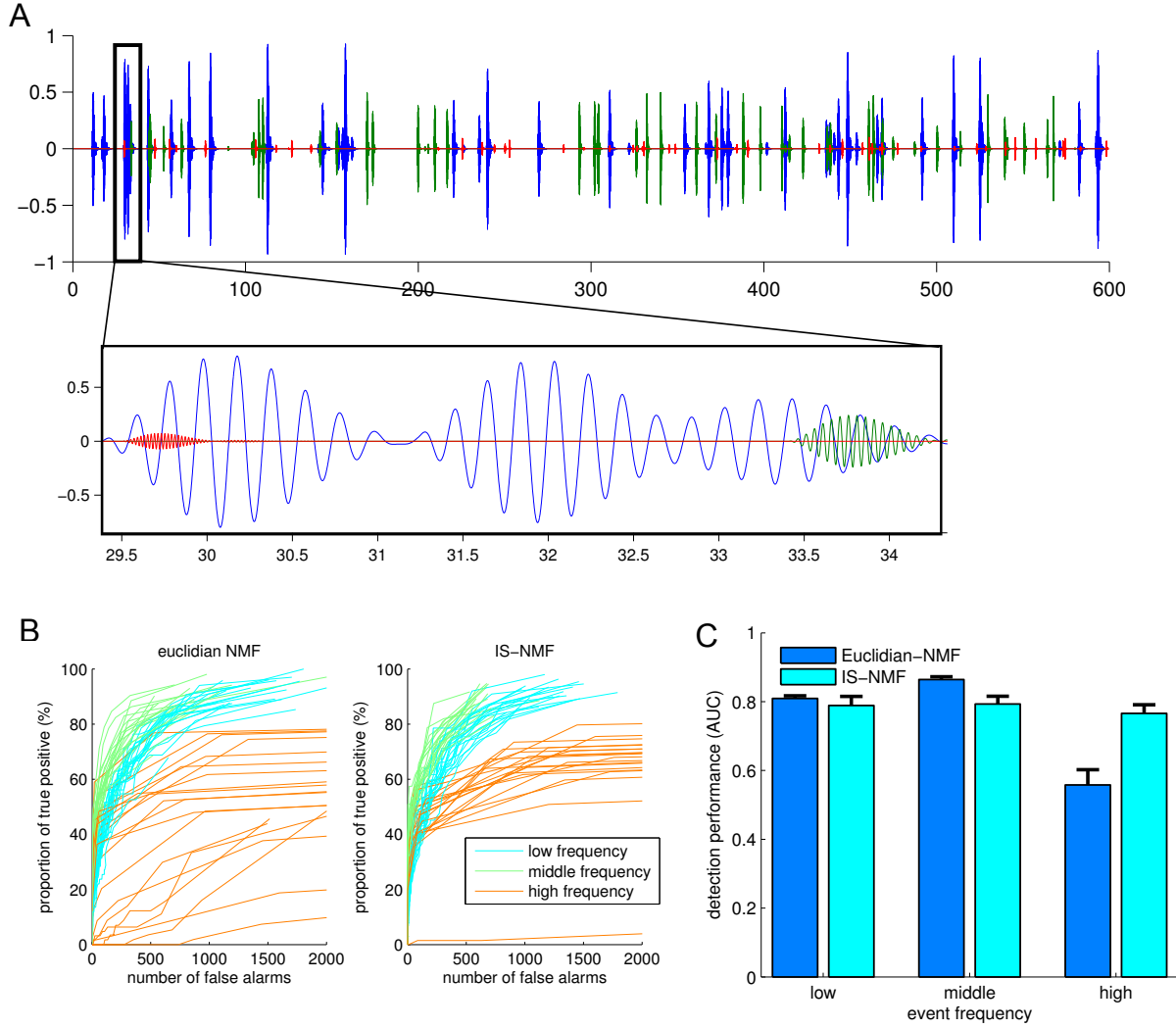
L. van der Maaten and G. Hinton. Visualizing Data using t-SNE. *J. Mach. Learn. Res.*, 9(86):2579–2605, 2008. ISSN 1533-7928.

A. Weigenand, M. S. Costa, H.-V. V. Ngo, J. C. Claussen, and T. Martinetz. Characterization of K-Complexes and Slow Wave Activity in a Neural Mass Model. *PLOS Computational Biology*, 10(11):e1003923, Nov. 2014. ISSN 1553-7358. doi: 10.1371/journal.pcbi.1003923.

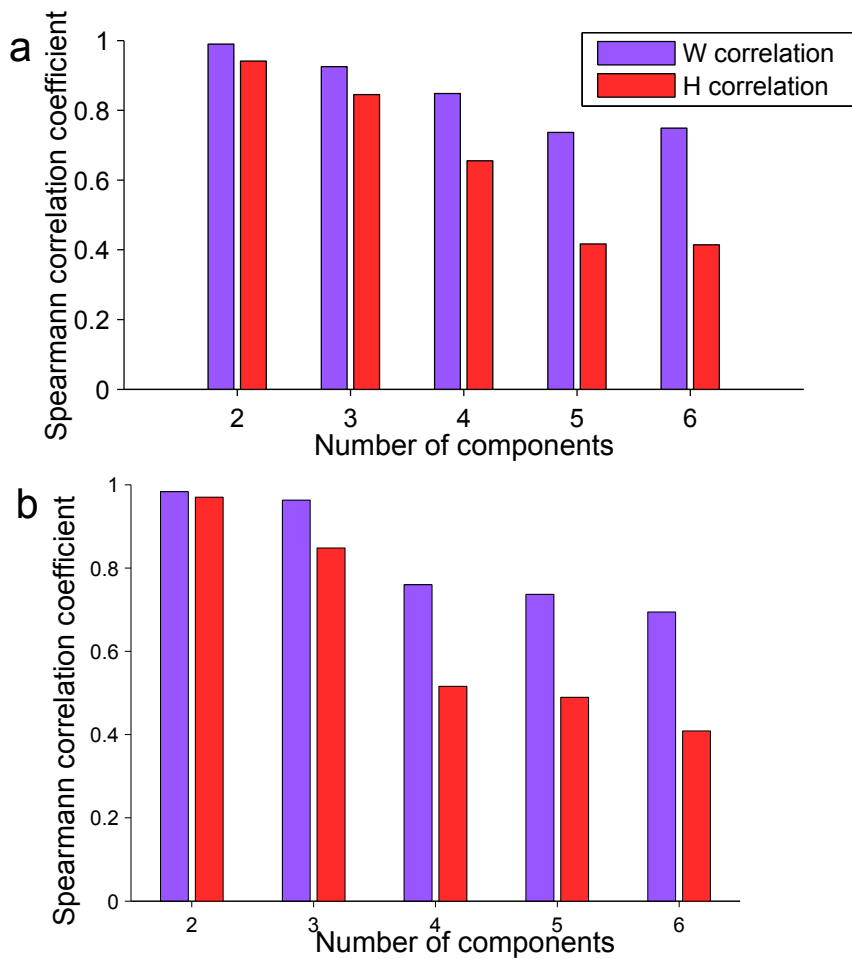
M. T. Wilson, J. W. Sleigh, D. A. Steyn-Ross, and M. L. Steyn-Ross. General Anesthetic-induced Seizures Can Be Explained by a Mean-field Model of Cortical Dynamics. *Anesthesiology*, 104(3):588–593, Mar. 2006. ISSN 0003-3022. doi: 10.1097/00000542-200603000-00026.



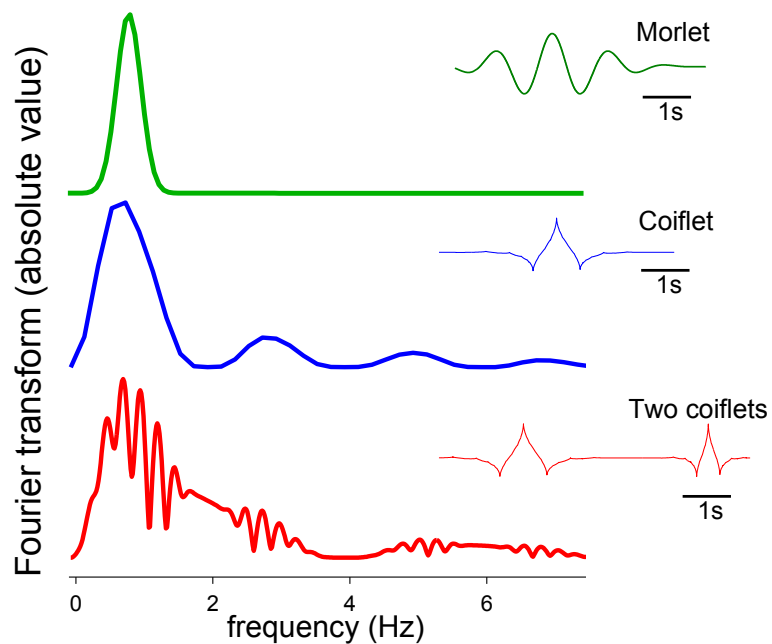
Supplementary Figure 1: Principle of the extraction of the time course of dynamical components based on NMF results. (a) For a given time window, the weighted spectral profiles of all NMF components are normalized for each frequency in order to sum to one. (b) These resulting functions are used as transfer functions in a filter bank of K filters, which are efficiently implemented as a simple multiplication in the frequency domain using the FFT algorithm. Activity of a given component is estimated by applying the corresponding filter to the LFP signal multiplied by a tapering function selecting the block of signal of current time window. Due to the normalization, the resulting sum of the time courses across all components reconstructs the original LFP signal. (c) The decomposition of panel b is implemented efficiently across the full time course of the signal using overlapping time windows, exemplified here with three time windows. The signal of each window is multiplied by a smooth tapering function such that the tapering coefficients of all overlapping windows at a given time point sum to one. This allows reconstructing without discontinuity the full time course of a component after filtering each frame independently by simply summing the filtered time courses contributed by each frame.



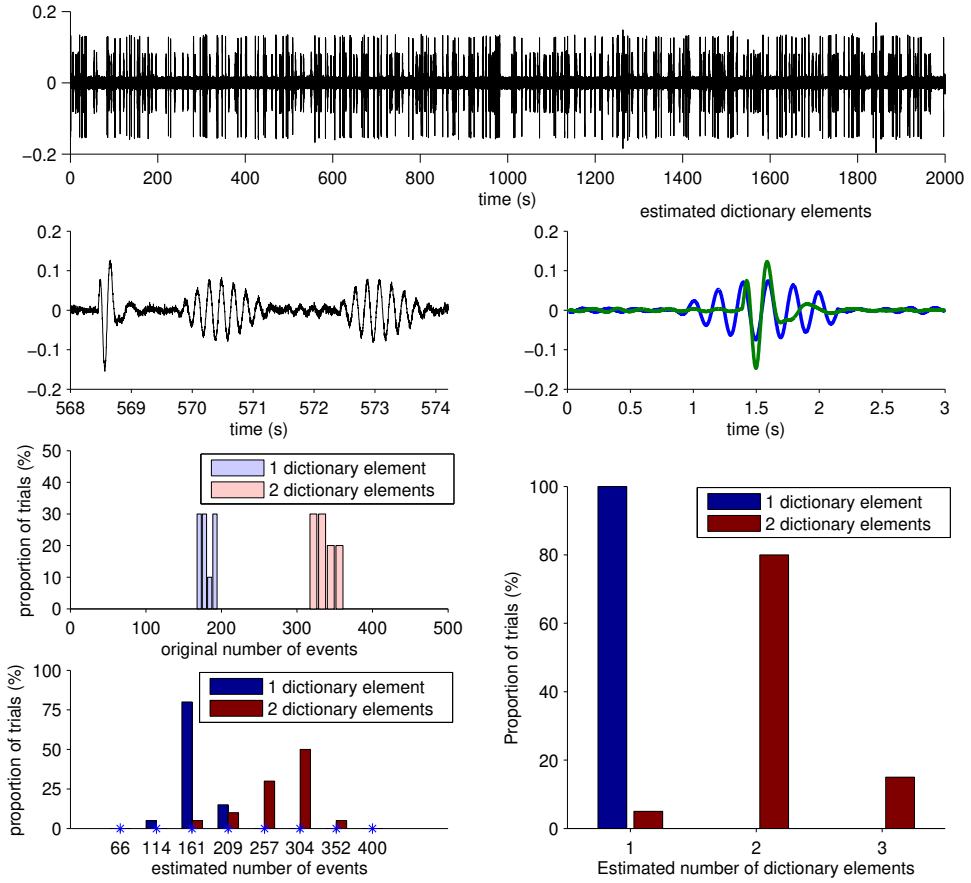
Supplementary Figure 2: **Comparison of Euclidean and Itakura-Saito NMF in simulation.** (a) Example time course of simulated dynamical components, representing low frequency (in blue), middle frequency (in green) and high frequency oscillations (in red). The inset represents a magnified version of the signals. (b) Spectral profiles associated to each components (estimated using the Welch periodogram). (c) Average cosine similarity between the original spectral profiles and those retrieved using Euclidean or Itakura-Saito NMF (error bars indicate standard deviation).



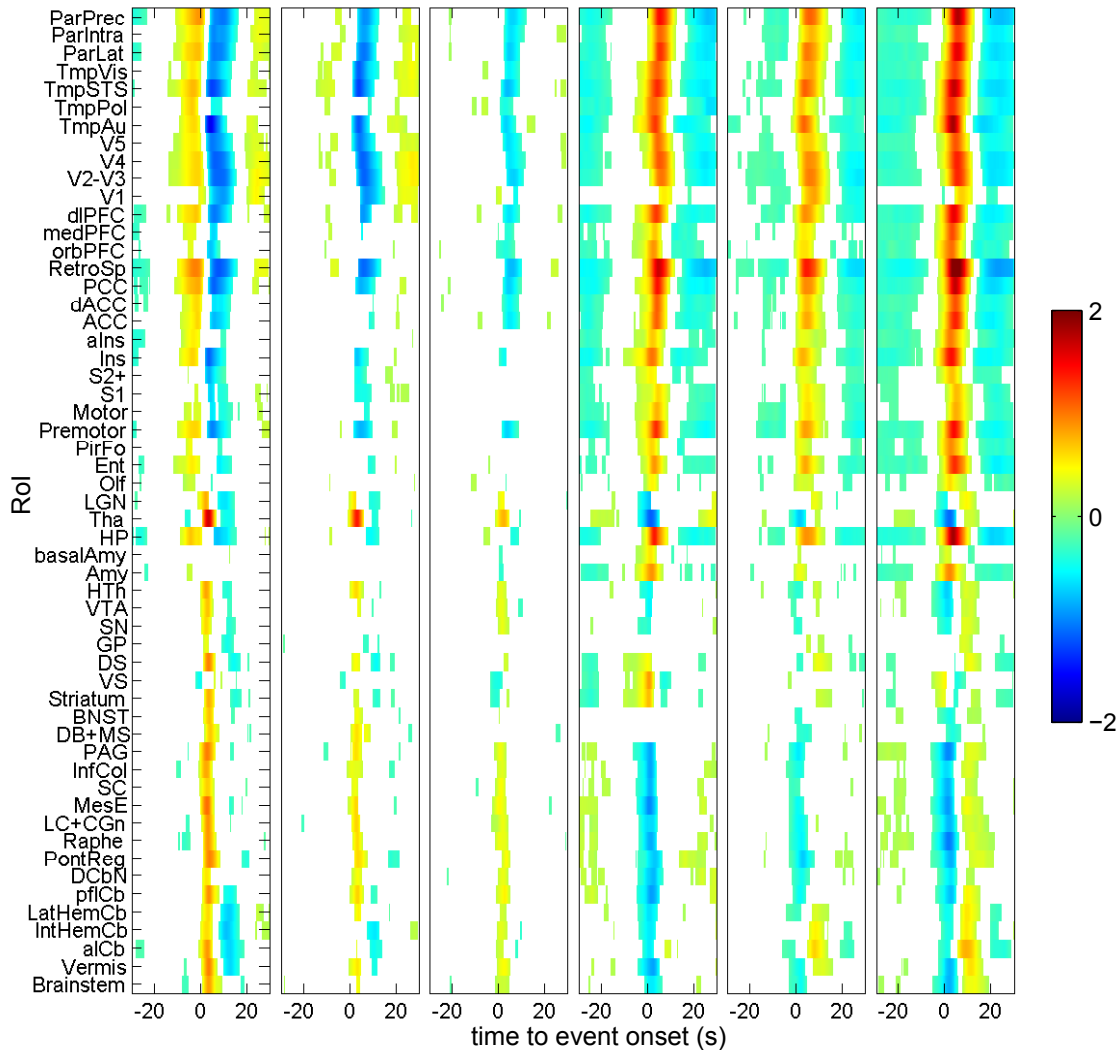
Supplementary Figure 3: **Selection of the number of NMF components.** (a) Average cosine similarity between bootstrapped NMF components averaged across all Hp recording sessions (blue: similarity between spectral profiles stored in the columns of the matrix \mathbf{W} , red: similarity between time-varying contribution of profiles to each time window stored in the lines of the matrix \mathbf{H}) (b) Average cosine similarity between bootstrapped NMF components averaged across all LGN recording sessions.



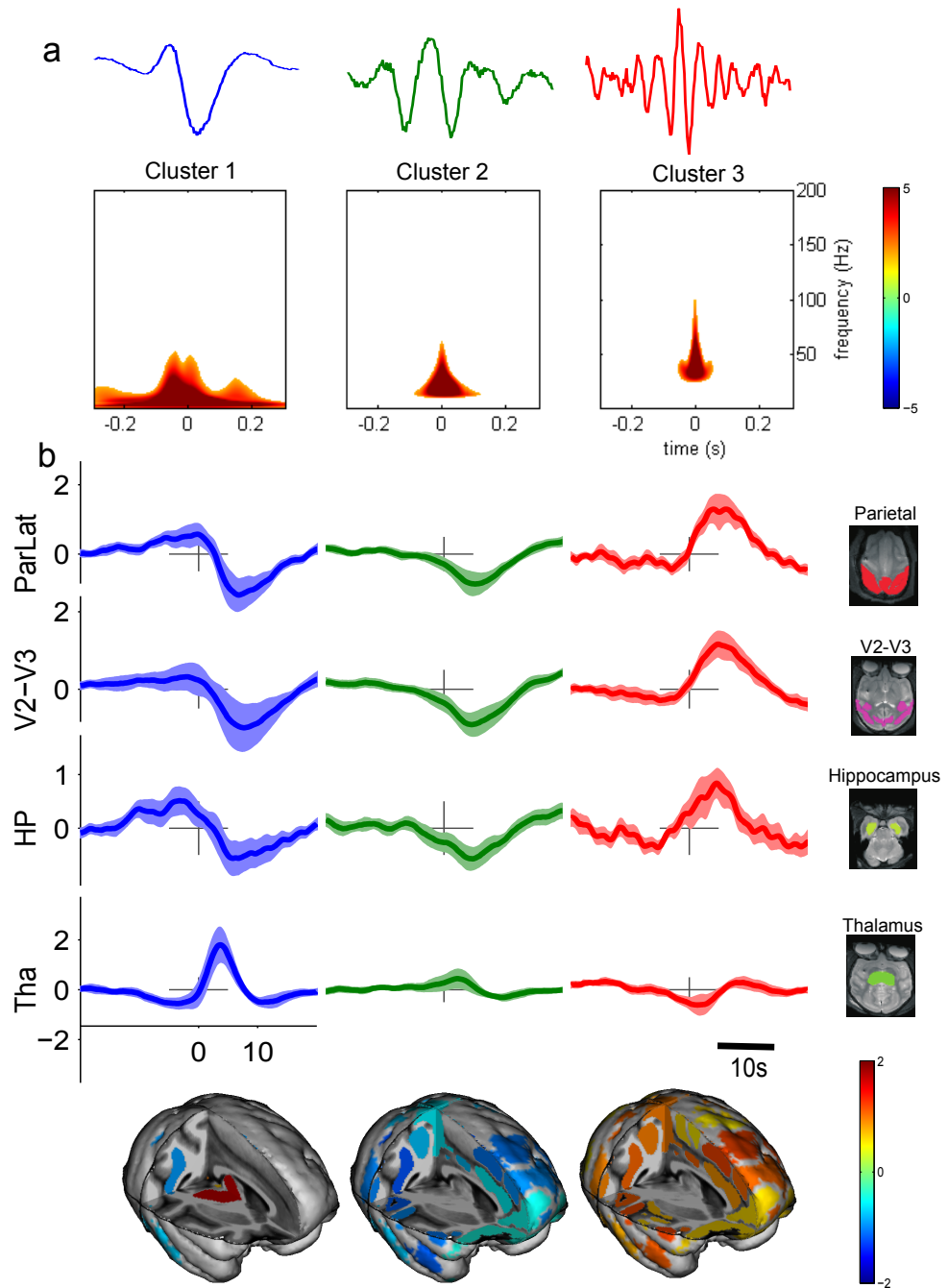
Supplementary Figure 4: **Properties of spectral profiles.** Absolute Fourier transform for different types of temporal patterns (see Supplementary Methods). Insets on the right hand side represent the time course of each pattern.



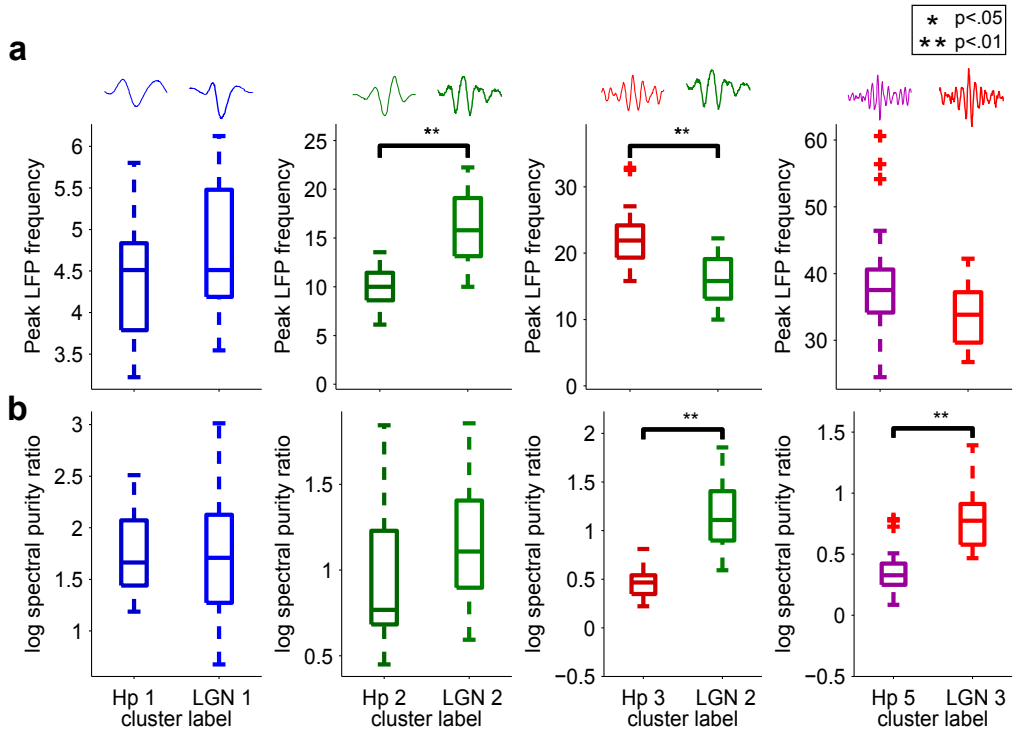
Supplementary Figure 5: **Dictionary learning.** (a) Example time course of a simulated time series with events taken from a dictionary with two patterns. (b) Magnified portion of time-course in (a) showing the occurrence of the first (blue arrow) and the second (green arrow) dictionary pattern. (c) Example of dictionary patterns estimated using our dictionary learning approach. (d) Histogram of the original number of events generated in simulations for two cases: events generated from one or two-patterns dictionary. (e) Histogram of the estimated number of events for both cases. (f) Estimated number of dictionary patterns estimated for both cases.



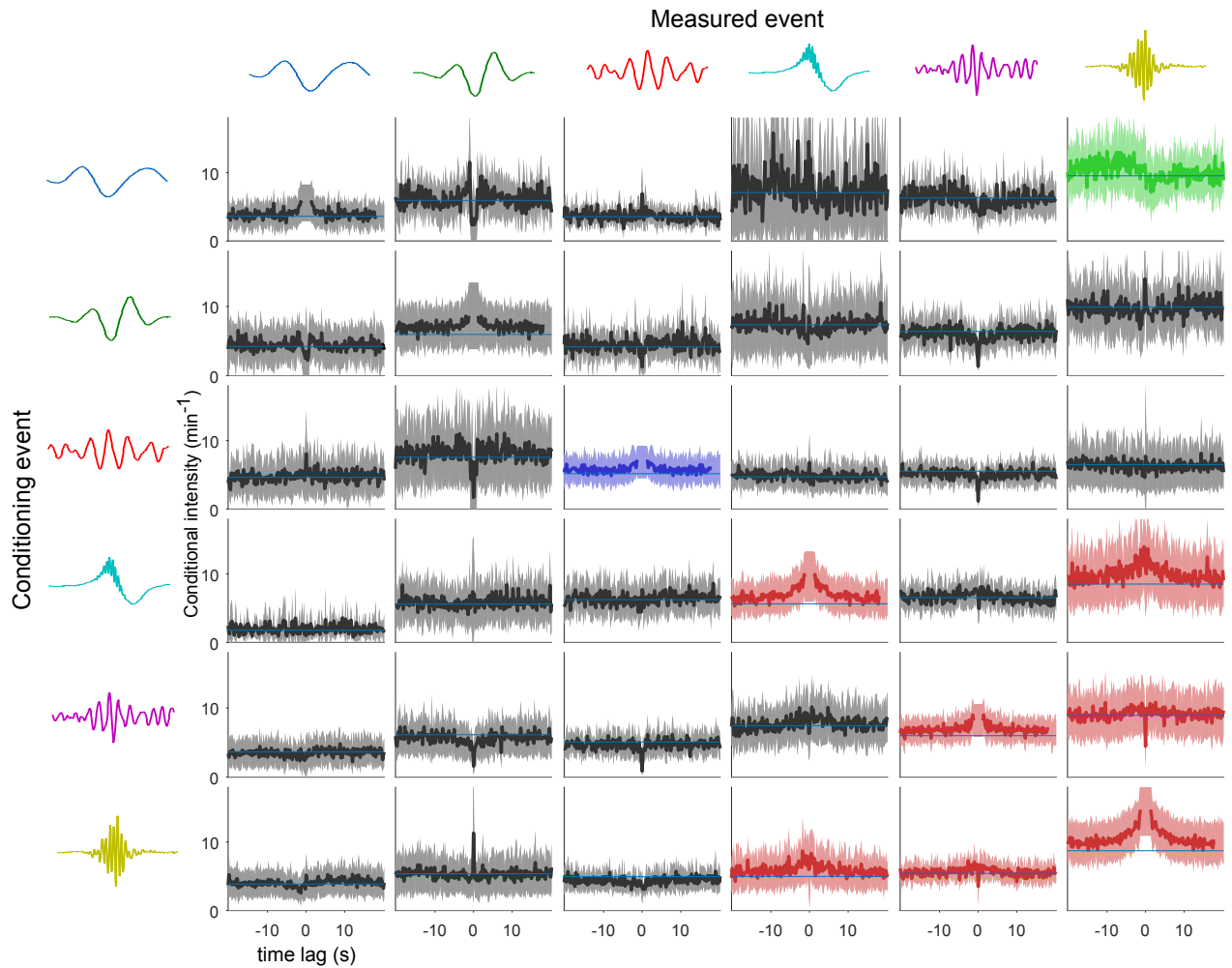
Supplementary Figure 6: Full NET-fmri response for hippocampal events. NET-fmri response averaged across voxels of each given ROI for each cluster of events. Rows indicate the considered ROI, columns indicate the cluster of events (same order as Figure 4). Values are z-scored with respect to randomized events. The meaning of Roi labels on the left hand side are detailed in Supplementary Table 1.



Supplementary Figure 7: Clustering of LGN events. (a-b) Average time-frequency map (a) and NET-fMRI (b) of the 3 clusters of LGN events (Z-score with respect to randomized event onsets). Waveforms in panel a are examples of learned dictionary patterns for each cluster. Bottom insets represent the trimensional mapping of the amplitude of this response at $t=3$ s overlaid on a template macaque brain.



Supplementary Figure 8: **Comparison of LGN and hippocampal event LFP properties.** (a) Comparison of the distribution of peak frequency of dictionary patterns originating from Hp and LGN structures. Horizontal lines indicate significant differences (Wilcoxon rank sum test; $p < .05$, Bonferroni corrected, from left to right: $n = 59, 58, 44, 43$). Traces at the top represent example dictionary patterns of each cluster. (b) Comparison of the distribution of log spectral purity ratio of dictionary patterns originating for Hp and LGN structures. Horizontal lines indicate significant differences (Wilcoxon rank sum test; $p < .05$, Bonferroni corrected, from left to right: $n = 59, 58, 44, 43$).



Supplementary Figure 9: **Conditional intensity of Hp events.** Estimated intensity of each type of event, conditioned on the occurrence of another type of event at time 0. Columns correspond to each event of which the rate is estimated, and lines indicate the event used for conditioning. Colored curves indicate significant average deviation of the intensity from baseline for different time intervals (Wilcoxon signed rank test; $p < .05$; FDR adjusted): red plots indicate change in the $[-3s, 3s]$ time window, excluding a $[-1s, 1s]$ interval and tested across all CA event pairs, blue plots indicate the same tested for all TA pairs, green curves indicate change in the $[-20s, -7s]$ interval tested across pairs of CA intensity, conditioned on TA events.

Group-ROI	Included Structures/Areas
V5	MT/MST
V4	V4 Complex
V2-V3	Areas V2/V3
V1	Primary Visual Cortex
ParPrec	Parietal Precuneus
ParIntra	Intraparietal Cortex
ParLat	Lateral Parietal
TmpVis	Inferotemporal Cortex
TmpSTS	Superior Temporal Sulcus
TmpAu	Temporal Auditory
TmpPol	Temporal Pole
dIPFC	Dorsolateral Prefrontal
medPFC	Medial Prefrontal
orbPFC	Orbitofrontal Cortex
S2+	Somatosensory Association
S1	Somatosensory Primate
Motor	Motor Cortex
Premotor	Premotor Cortex
RetroSp	Retrosplenial Cortex
PCC	Posterior Cingulate
ACC	Anterior Cingulate
Ins	Insular Cortex
Olf	Olfactory Cortex
PirFo	Piriform Cortex

Group-ROI	Included Structures/Areas
Ent	Entohinal Cortex
HP	Hippocampus
Amy	Amygdala
HTh	Hypothalamus
Septum	Septum
DB	Diagonal Band
GP	Glovus Pallidus
Striatum	Striatum
LGN	Lateral Geniculate Nucleus
Tha	Thalamus
VTA	Ventral Tegmental Area
SN	Substantia Nigra
LC+CGn	Locus Coeruleus – Cent Gray
PAG	Periaqueductal Gray
InfCol	Inferior Colliculus
SC	Superior Colliculus
Raphe	Raphe Nuclei
PontReg	Pontine Region
alCb	Anterior Cerebellar Lobe
DCbN	Deep Cerebellar Nuclei
pflCb	Paraflculonodular Cerebellum
LatHemCb	Lateral cereb. hemisphere
IntHemCb	Intermediate cer. hemisphere
Vermis	Vermis

Supplementary Table 1: **ROI labels.** Nomenclature of the ROIs used in the present study. The two columns show respectively the utilized group ROI labels and the cortical or subcortical regions that they include. More information can be found in (Logothetis et al. 2012).